(12) INTERNATIONAL APPLICATION PUBLISHED UNDER THE PATENT COOPERATION TREATY (PCT)

(19) **World Intellectual Property Organization**
International Bureau

(43) **International Publication Date**
9 July 2015 (09.07.2015)

WIPO | PCT

(10) **International Publication Number**
WO 2015/103199 A1

(51) **International Patent Classification**:
F25B 15/06 (2006.01) ***F25B 17/00*** (2006.01)
F25B 15/16 (2006.01)

(21) **International Application Number**:
PCT/US2014/072664

(22) **International Filing Date**:
30 December 2014 (30.12.2014)

(25) **Filing Language**: English

(26) **Publication Language**: English

(30) **Priority Data**:
61/922,460 31 December 2013 (31.12.2013) US

(71) **Applicant**: **UNIVERSITY OF FLORIDA RESEARCH FOUNDATION, INC.** [US/US]; 223 Grinter Hall, Gainesville, FL 32611 (US).

(72) **Inventors**: **MOGHADDAM, Saeed**; 4235 S.w. 96th Drive, Gainesville, FL 32608 (US). **CHUGH, Devesh**; 3800 S.w. 34th Street, Apt. T181, Gainesville, FL 32608 (US). **BIGHAM, Sajjad**; 704 S.w. 16th Avenue, Apt. 211, Gainesville, FL 32601-8581 (US).

(74) **Agents**: **BUESE, Mark, A.** et al.; Saliwanchik, Lloyd & Eisenschenk, P.O. Box 142950, Gainesville, FL 32614-2950 (US).

(81) **Designated States** *(unless otherwise indicated, for every kind of national protection available)*: AE, AG, AL, AM, AO, AT, AU, AZ, BA, BB, BG, BH, BN, BR, BW, BY, BZ, CA, CH, CL, CN, CO, CR, CU, CZ, DE, DK, DM, DO, DZ, EC, EE, EG, ES, FI, GB, GD, GE, GH, GM, GT, HN, HR, HU, ID, IL, IN, IR, IS, JP, KE, KG, KN, KP, KR, KZ, LA, LC, LK, LR, LS, LU, LY, MA, MD, ME, MG, MK, MN, MW, MX, MY, MZ, NA, NG, NI, NO, NZ, OM, PA, PE, PG, PH, PL, PT, QA, RO, RS, RU, RW, SA, SC, SD, SE, SG, SK, SL, SM, ST, SV, SY, TH, TJ, TM, TN, TR, TT, TZ, UA, UG, US, UZ, VC, VN, ZA, ZM, ZW.

(84) **Designated States** *(unless otherwise indicated, for every kind of regional protection available)*: ARIPO (BW, GH, GM, KE, LR, LS, MW, MZ, NA, RW, SD, SL, ST, SZ, TZ, UG, ZM, ZW), Eurasian (AM, AZ, BY, KG, KZ, RU, TJ, TM), European (AL, AT, BE, BG, CH, CY, CZ, DE, DK, EE, ES, FI, FR, GB, GR, HR, HU, IE, IS, IT, LT, LU, LV, MC, MK, MT, NL, NO, PL, PT, RO, RS, SE, SI, SK, SM, TR), OAPI (BF, BJ, CF, CG, CI, CM, GA, GN, GQ, GW, KM, ML, MR, NE, SN, TD, TG).

Published:

— *with international search report (Art. 21(3))*

(54) **Title**: 3D MICROCHANNEL STRUCTURES FOR MEMBRANE ABSORPTION/DESORPTION

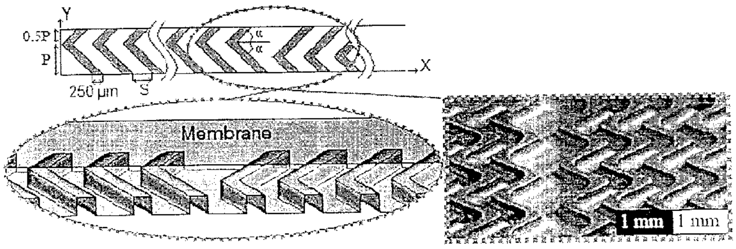

Figure 8

(57) **Abstract**: An absorber or desorber contains one or more micro-channels that have a 3-D structured heat-exchanging surface and a membrane on the microchannel situated distal to the 3-D structured heat-exchanging surface, where the membrane is permeable to a solvent of a solution employed in the absorber or desorber. The 3-D structured surface promotes mixing of hot and cold solution between the 3-D structured heat-exchanging surface and a vapor- exchanging surface proximal to the membrane. The mixing reduces the differences in concentration and temperature of the bulk solution and the solution at the vapor-exchanging surface to enhance the efficiency and rate of absorption or desorption of the solvent.

WO 2015/103199 A1

DESCRIPTION

3D MICROCHANNEL STRUCTURES FOR MEMBRANE ABSORPTION/DESORPTION

CROSS-REFERENCE TO RELATED APPLICATION

The present application claims the benefit of U.S. Provisional Application Serial No. 61/922,460, filed December 31, 2013, which is hereby incorporated by reference herein in its entirety, including any figures, tables, or drawings.

This invention was made with government support under 00104171 awarded by the Department of Energy. The government has certain rights in the invention.

BACKGROUND OF INVENTION

Absorption and/or desorption are processes that are exploited in many processes. These processes involve the gain or loss of a component to a solution. Many factors affect these processes, including solution compositions, heat exchange, surface area, temperatures, and other factors. Many absorption and desorption processes involve aqueous solutions.

Absorption of species into a liquid is widely used in many technologies, including: absorption heat pumps; liquid desiccant-based dehumidification; purification of the natural gas streams involving separation of CO_2 and H_2S; removal of CO_2 from flue gas; and bioreactors in which gaseous products are absorbed into a liquid phase for processing/conversion by microorganisms. Absorption is limited by the rate of absorbate diffusion into the absorbent. In cases involving an absorbate with a high heat of phase change, such as water vapor absorption into a lithium bromide (LiBr) solution in an absorption heat pump or a dehumidifier, the absorption rate is also limited by thermal diffusion. When the heat released at the vapor-liquid interface due to phase change is not removed, there is an increase in temperature and equilibrium water vapor pressure at the interface. This increase in water vapor pressure lowers the rate of water vapor absorption.

Enhancement of water vapor absorption rates into LiBr have been pursued, yet few tangible results have been achieved due to the challenges of controlling thermohydraulic characteristics of a falling LiBr solution film. Yu *et al.*, “Parametric Study of Water Vapor

Absorption Into a Constrained Thin Film of Lithium Bromide Solution" *International Journal of Heat and Mass Transfer* 2012, *55*, 5687–95 discloses a numerical model for the absorption characteristics of LiBr solution flows and that heat and mass transfer limits in a LiBr solution flow could be enhanced in flow channels with thicknesses less than a few hundred microns when employing high flow velocities. Thin solution flow reduces the heat diffusion path to the cooling surface beneath the solution film and a high solution flow velocity diminishes the thickness of any concentration boundary layer. Nasr *et al.* "Absorption Characteristics of Lithium Bromide (LiBr) Solution Constrained by Superhydrophobic Nanofibrous Structures" *International Journal of Heat and Mass Transfer* 2013, *63*, 82–90 disclosed an experimental study where a LiBr solution flow is constrained by a superhydrophobic nanofibrous membrane with the absorption characteristics could be modified by control of the flow thickness and flow velocity to significantly increase absorption rates over those of falling films, where a solution film thicknesses on the order of about 100 μm was found to give superior results. However, the manifolding burden of an absorber having such a thin solution flow channel is high and tends to limit the capacity of the absorber. Hence, one is typically obliged to reduce the flow pressure drop by increasing the solution channel thickness, as flowing a fixed amount of mass through a 100 μm thick channel has approximately a 125 times greater pressure drop than that of a 500 μm thick channel. However, increasing the solution channel thickness also reduces the absorption rate, since transport within the solution flow as molecular diffusion is the sole mechanism for the absorbed molecule to be transported into the bulk absorbent, and mixing is needed to achieve high absorption rates.

Common desorbers for absorption refrigeration systems (ARSs) involve nucleate pool boiling or falling films over horizontal or vertical tubes are the common configurations in lithium bromide (LiBr). In the pool boiling configuration, water is boiled from a pool of LiBr solution. In a falling film desorber, a LiBr solution is sprayed over a tube bundle while the heating medium flows inside the tubes. At low surface temperatures, water directly diffuses from the solution film when the solution temperature remains sufficiently high to sustain a solution water vapor pressure above the external vapor pressure. When the wall temperature sufficiently exceeds the solution saturation temperature, desorption also takes place from bubble nuclei formed at the solid-liquid interface.

A superheat temperature, which is the difference between the wall and solution saturation temperatures, of approximately 10 °C is required for boiling inception. Water bubble growth rate is significantly slow in in the LiBr solution because of the low water diffusion coefficient in the solution. As in pure water, bubble growth in LiBr solution is limited by mass diffusion rather than by heat transfer. Consequently, a significant surface superheat temperature is required to grow bubbles where the buoyancy force overcomes the surface tension and departure from the heat transfer surface.

An increase in the desorption rate and a reduction of the required surface superheat temperature are desirable for reducing the size of a desorber and lowering its heating medium temperature. For example, the use of an absorption cycle with solar-thermal collectors or photovoltaics with waste heat recovery is benefitted by a reduction of the required heat source temperature to enhance the prospect of directly converting solar heat into a cooling effect.

Mixing has been examined in laminar flow microchannels involves inclusion of active or passive components. Active mixers, such as piezoelectric and magneto/electrohydrodynamic actuators or pressure perturbers place additional burden on the system. A passive approach is disclosed in Stroock *et al.* Chaotic Mixer for Microchannels" *Science* 2002, *295*, 647–51 where chaotic advection is generated within the flow through stretching and folding the laminar streamlines due to ridges formed in the base of a channel. This passive mixture was employed to mix streams of liquids that are introduced at an inlet to an enclosed channel. The effect of such mixers on absorbers and desorbers where a vapor is included or excluded over the length of the channel has not been examined.

BRIEF DESCRIPTION OF DRAWINGS

Figure 1 show a 3D schematic of 3D-structured surface features and a fluid particle trajectory, streamline, as it enters and exits the spacing between the surface features and generates a z-direction velocity component in absorbers and desorbers, according to embodiments of the invention.

Figure 2 shows a photograph of the assembled ARS-like system employed in an experimental setup using an absorber, according to an embodiment of the invention.

Figure 3 shows a photograph of an absorber, according to an embodiment of the invention, having a PTFE membrane bonded over its vapor-exchanging surface.

Figure 4 shows plots of absorption rate as a function of a) vapor pressure and b) cooling water temperature and c) a plot of absorption rate, as a function pressure potential, of base case absorbers, and absorbers, according to an embodiment of the invention, with comparison to prior art absorbers.

Figure 5 shows a map of a) LiBr solution concentration and b) temperature contours within a 500-micron-thick and 600-mm-long flow channel for a base case simulation lacking 3D-structures, using parameters provided by Table 2 as input to the simulation.

Figure 6 shows a plot of the variations of temperature and concentration at the vapor-exchanging surface, labeled interface, and within the bulk along the flow channel of a base case absorber.

Figure 7 shows a plot of the variations of absorption rate along the length of a base case solution channel.

Figure 8 shows a top view indicating the geometric features tabulated in Table 3, a 3D schematic of a flow channel with a 3D-structured heat-exchanging surface showing the ridges, and a photograph of a herringbone 3D-structured heat-exchanging surface made of cupper through a wet etching process, for absorbers and desorbers, according to embodiments of the invention.

Figure 9 shows a 3D projection of concentration contours including two vortices formed on the short and long arms of the micro-ridge of a channel of a 3D structured absorber, according to an embodiment of the invention.

Figure 10 shows a plot of the variations of y and z components of the velocity vector along a microchannel at $y = 180\ \mu m$ and $z = 750\ \mu m$ for channels of a base case and channels with and without thermally conductive sidewalls, according to embodiments of the invention.

Figure 11 shows a map of a) LiBr solution concentration and b) temperature contours within a 500-micron-thick and 600-mm-long flow channel incorporating micro-ridges on the heat-exchanging surface of the channel of an absorber, according to an embodiment of the invention, using parameters provided in Table 2 as input to the simulation.

Figure 12 shows a plot of temperature and LiBr concentration at the vapor-exchanging surface, labeled interface, and within the bulk solution along a flow channel incorporating micro-ridges on the heat-exchanging surface, according to an embodiment of the invention.

Figure 13 shows plots of the absorption rate along the length of absorbers for a base case absorber, an absorber with 3D-structured ridges, according to an embodiment of the invention, and an absorber with 3D-structures and thermally conductive walls, according to an embodiment of the invention.

Figure 14 shows a plot of the temperature and concentration at the vapor-exchanging surface, labeled interface, and in the bulk solution along the length of the flow channel having 3D-structured ridges and heat conducting sidewalls, according to an embodiment of the invention.

Figure 15 shows a schematic diagram of an exemplary desorber that can employ a 3D-structured heat-exchanging surface, according to an embodiment of the invention.

Figure 16 shows plots of desorption rates versus heat-exchanger, labeled wall temperature, at different vapor and solution pressures, where SPh and TPh stand for single-phase and two-phase desorption modes, respectively and the dash lines mark where a significant change in the rate of increase in desorption occurs that indicates a shift from SPh to TPh desorption mode in base case desorbers and desorbers, according to an embodiment of the invention.

Figure 17 shows plots of calculated solution water vapor pressure, $P_{s,w}$, as a function of temperature and LiBr concentration and the solution saturation temperature, T_{sat}, as a function of solution pressure and concentration.

Figure 18 shows a map of LiBr solution concentration contours within a 200 µm thick and 89 mm long channel in a base case desorber.

Figure 19 shows i) a staggered herringbone 3D-structured heat-exchanging surface with micro-ridges for a desorber, according to an embodiment of the invention, and ii) two fluid vortex pathlines during a simulated solution flow.

Figure 20 shows i) a 3D view of LiBr concentration contours for a channel of a desorber according to an embodiment of the invention and ii) LiBr concentration cross-sections at various lengths between an inlet, x=0, and 29 mm along a channel of the desorber.

Figure 21 shows a map of LiBr solution concentration contours within a 200 µm thick and 89 mm long channel having 3D-structured micro-ridges on the heat-exchanging surface at the flow channel bottom, according to an embodiment of the invention.

Figure 22 shows plots of the desorption rate (J) of a desorber according to an embodiment of the invention, and the concentration (C) and temperature (T) in the bulk solution and at the vapor-exchanging surface, labeled interface, along the length of the flow channel.

DETAILED DISCLOSURE

Embodiments of the invention are directed to absorbers and to desorbers that comprise a membrane over a microchannel that is three-dimensionally structured on at least the heat-exchanging surface to promote vortices for mixing of the temperatures and concentrations between the heat-exchanging and vapor-exchanging surfaces. These membrane absorbers and desorbers allow vapors to enter or exit the absorbers or desorbers, respectively, while retaining the flowing liquid. The 3D structured surfaces overcome diffusion limitations by incorporation of a textured surface, for example, one with staggered herringbone structures, and hereafter called “ridges”, on the heat-exchanging surface, which is the flow channel’s bottom wall.

The ridges of the 3D-structured surface generate anisotropic resistance to the absorbent or desorbent flow, which stretches and twists portions of the volume of the flowing solution. Ridges of a few hundred microns in depth induce surface vortices with sufficient momentum to impact the main flow and continuously replenish the vapor-exchange surface with a concentrated solution. An exemplary 3D-structured surface that is conducive to the transfer of dilute and concentrated solution from the heat-exchanging surface to the vapor-exchanging surface is shown in Figure 1.

By inducing the mixing of concentrated and dilute solutions of different temperatures, the efficiency of an absorber or desorber can be significantly improved relative to a base case, which lacks a 3D-structured heat-exchanging surface on the base of the microchannels. The ridges promote uniformity in the concentrations and temperatures across the cross-sectional area of the micro-channels proceeding down the length of the channels. In an embodiment of the invention, walls that are perpendicular to the heat-exchanging and vapor-exchanging surfaces can be thermally conductive to further enhance the temperature homogeneity possible in the channels. Such absorbers and desorbers are advantageous for use in absorption refrigeration systems (ARSs) and other applications.

METHODS AND MATERIALS

Numerical Simulations

To formulate the problem, a continuum-based approach is used to asses the absorption/desorption process involved in 3D structured membrane absorbers/desorbers, according to embodiments of the invention. Fluid flow is modeled as steady, laminar, and incompressible. The governing equations can be written as:

$$u_j \frac{\partial u_i}{\partial x_j} = -\frac{1}{\rho}\frac{\partial p}{\partial x_i} + \nu \frac{\partial u_i}{\partial x_j \partial x_j} \qquad (1)$$

$$u_j \frac{\partial T}{\partial x_j} = \alpha \frac{\partial T}{\partial x_j \partial x_j} \qquad (2)$$

$$u_j \frac{\partial X}{\partial x_j} = D \frac{\partial X}{\partial x_j \partial x_j} \qquad (3)$$

where u is the velocity, ρ is the solution density, ν is the kinematic viscosity, p is the fluid pressure, T is the solution temperature, α is the thermal diffusivity, C is the solution concentration and D is the mass diffusivity. For example, in a membrane absorber, the vapor has to pass through the membrane pores before contacting the LiBr solution. Flow through a porous membrane can be classified as viscous, transitional, or free molecular flow regimes depending on the magnitude of the Knudsen (Kn) number. Kn number is defined as the ratio of the mean free path (λ) to the pore diameter (d_p):

$$Kn = \frac{\lambda}{d_p} \tag{4}$$

The mean free path is given by:

$$\lambda = \frac{k_b T}{\sqrt{2}\pi d^2 p} \tag{5}$$

where k_b is the Boltzmann constant, T is the absolute temperature, d is the molecular diameter, and p is the vapor pressure. To calculate mass flux through the membrane, the flow regime must be established. The flow regime for a free molecular regime is characterized by $Kn > 10$ and a transitional flow regime exists for $0.1 < Kn < 10$. The vapor pressure at 5 $^\circ C$, which is the operating temperature of a typical evaporator, is 873 Pa. The diameter of the water molecule is 2.7×10^{-10} m. These values yield a water molecule mean free path of 13 μm. As the optimal membrane pore size for an absorber application is anticipated to be less than 1 μm such membranes posses a reasonable liquid breakthrough pressure with a vapor flow through the membrane pores in the transitional or free molecular flow regime. According to the Dusty-Gas model, mass transfer through a membrane consists of diffusion and viscous fluxes where the molar diffusion flux is given by:

$$N^D = D_e^k \frac{-1}{RT} \Delta p \tag{6}$$

$$D_e^k = \frac{2\varepsilon r}{3\tau} \sqrt{\frac{8RT}{\pi M}} \tag{7}$$

where R is the gas constant, M is the molecular weight, r is the pore radius, ε is the membrane porosity, and τ is the membrane tortuosity. The molar viscous flux is given by:

$$N^V = \frac{-p}{RT\mu} \frac{\varepsilon r^2}{8\tau} \Delta p \tag{8}$$

where μ is the viscosity and p is the pressure. The total mass flux through the membrane pores can be written as the sum of the diffusion and viscous fluxes:

$$N = N^D + N^V \tag{9}$$

The vapor mass flux through the membrane can be then computed from:

$$J = k_m(p_v - p_i),\ k_m = -\frac{M}{\delta_m}(\frac{D_e^k}{RT} + \frac{pB_0}{RT\mu}) \tag{10}$$

where k_m is the membrane mass transfer coefficient or permeability, p_v is the water vapor pressure, p_i is the water vapor pressure of the solution at the interface and δ_m is the membrane thickness.

To evaluate the accuracy of Equation 10, permeability of nanofibrous membranes with different pore sizes were experimentally measured. Nanofibrous membrane with a pore size of 1 μm has a relatively low pressure drop compare to the overall pressure potential that drives the absorption process. Tests were performed at a flow rate of up to 0.01 $kg\ m^{-2}s^{-1}$ and an absolute pressure of 0.85 *kPa*. The results are within 5% of those predicted by Equation 10. Measurements on a 160-μm-thick solution film over an absorption rate of 0.002-0.006 $kg\ m^{-2}s^{-1}$ suggested that the dominant resistance is mass transfer through the solution (P_i–P_s) and membranes only contribute approximately 20% to the overall resistance.

Modeling assumes that the LiBr solution and the vapor are in an equilibrium state at the membrane surface. Mass fluxes across the membrane and heat transfer to the vapor phase through the membrane are assumed to be negligible compared to mass flux along the channel. Therefore, the heat and mass boundary conditions at the membrane surface are:

$$k(T,X)\frac{\partial T}{\partial n} = h(T,X).k_m(p_v - p_i(T,X)) \tag{11}$$

$$D(T,X).\rho(T,X)\frac{\partial X}{\partial n} = k_m(p_v - p_i(T,X)) \tag{12}$$

where h is the latent heat of evaporation, ρ is the solution density, and n is the interface normal direction. LiBr properties are those reported by McNeely, "Thermodynamic Properties of Aqueous Solutions of Lithium Bromide", ASHRAE Trans 1979, *85*, 413–34.

No-slip and no-flux boundary conditions are used for momentum and the concentration equations, respectively, at the heat exchanging surface with a linear temperature distribution. The temperature and concentration are specified at the inlet and a zero gradient boundary condition was used for the temperature and the concentration at the outlet. Symmetric conditions are applied on the sides of the flow domain.

To solve the governing equations (1-3) with the boundary conditions, an in-house computational fluid dynamics solver based on the Lattice Boltzmann Method (LBM) was used with a finite difference method for the concentration and temperature fields. In the LBM, the fluid is simulated by fictive particles with a mass distribution function of

$f(\vec{x}, \vec{e}, t)$. The motion of these particles is set from the solution of the Boltzmann equation with BGK approximation over a discrete lattice mesh. The popular single relaxation time (SRT) model, with the time step δt and space step e_α δt, is:

$$f_\alpha(X_i + e_\alpha \delta t, t + \delta t) - f_\alpha(X_i, t) = -\frac{1}{\lambda}\left[f_\alpha(X_i, t) - f_\alpha^{(eq)}(X_i, t)\right] \tag{13}$$

where e_α is the discrete particle velocity set, λ the normalized relaxation time, and X_i a point in the discretized physical space. The viscosity in the N–S equation derived from Equation (13) is:

$$\nu = \left(\lambda - \frac{1}{2}\right) c_s^2\, \delta t \tag{14}$$

where C_s is the speed of sound, where this choice of the viscosity makes formally the LBGK scheme a second order method for solving incompressible flows. The positivity of the viscosity requires that $\lambda > 0.5$. The term $f_\alpha(Xi,\ t)$ is the discretized distribution function associated with the α-th discrete velocity e_α and $f_\alpha^{(eq)}$ is the corresponding equilibrium distribution function. The macroscopic quantities, such as mass density ρ and momentum density ρu, can be obtained by evaluating the hydrodynamic moments of the distribution function f as follows:

$$\rho = \sum_\alpha f_\alpha^{eq} \tag{15}$$

$$\rho \vec{u} = \sum_\alpha f_\alpha^{eq} \vec{e}_\alpha \tag{16}$$

The grid dimensions of the computational domain were 5 μm in all three directions. A grid independence study was performed to ensure that the computational results are independent of the grid size. The maximum error in the absorption rate was found to be less than 2% when the grid size was reduced by a factor of 2.

Figure 2 depicts a photograph of an exemplary setup used for generation of experimental data, with an absorber, according to embodiments of the invention. The experimental loop consists of a LiBr solution line and a refrigerant, water, line. The solution line consists of an absorber, desorber, pump, filter, solution reservoir, Coriolis mass flow meter, and two solution heat exchangers. A photograph of the absorber with a polytetrafluoroethlyene (PTFE) membrane bonded over its surface is shown in Figure 3. The water line consists of an evaporator, condenser, Coriolis mass flow meter, and a water reservoir. In the solution line, a micro gear pump (HNP Mikrosysteme, Germany) drives the weak LiBr solution to a Coriolis mass flow meter (Bronkhorst, USA) into and through a solution heat exchanger where the solution is preheated to a desired temperature before entering the desorber. In the desorber, the weak LiBr solution is heated by a thin film heater (Omega Engineering, CT) to desorb water. The desorbed water vapor flows to a condenser and the strong LiBr solution exits the desorber and flows through a heat exchanger, where it is cooled to a preset temperature before it enters the absorber. The condensed water leaves the condenser and flows through a Coriolis mass flow meter (Micro Motion, CO) to the evaporator, where it is vaporized as the vapor supplied to the absorber. The concentrated solution flows through the absorber, absorbing the water vapor generated in the evaporator. The dilute solution leaving the absorber flows through a filter and is pumped back to the solution pre-heater and the desorber to complete the cycle. The desorber and evaporator heat exchangers are heated by flexible heaters. The experimental loop is equipped with two small reservoirs with sight glass to monitor the liquid in the solution and in the water lines. These reservoirs serve as compensation chambers and assist in charging of the loop. The data are measured by pressure transducers, thermocouples, and mass flow meters; and are recorded by a data acquisition system.

The system solution loop was charged with a 55% LiBr solution inhibited by Lithium Molybdate (Leverton-Clarke Ltd, UK). The water line was charged with degassed and deionized water. Each experimental run began by operating the solution pump and setting the flow rate to a desired value. Subsequently, the water chiller was turned on and the temperature of the absorber cooling water was set. A valve between the evaporator and absorber was then opened to begin the absorption process. Next, the TEC modules were turned on and the inlet temperatures to the absorber and desorber heat exchanges were set. Once the desired temperatures were reached, the desorber and evaporator heaters were powered. Changes in temperatures, pressures, and mass flow rates were monitored continuously. The system was assumed to have reached steady-state when variations in the absorber pressure and the solution density were within 10 Pa and 5 kg/m^3, respectively, for at least 30 minutes. The absorption rate was directly measured by the water line mass flow meter.

The accuracy of the water mass flow meter that directly measures the water absorption rate is ±1%. However, due to the unsteady nature of the condensate flow, a fluctuation of up to ±5% was recorded during the experiment. The reported absorption rates are the average of the measured values over a period of time, after the system reached a steady state. The concentration uncertainty is calculated using the following equation:

$$\Delta X = \sqrt{\left(\frac{\partial X}{\partial \rho}\Delta \rho\right)^2 + \left(\frac{\partial X}{\partial T}\Delta T\right)^2}$$

where X and T are the solution concentration and temperature, respectively, and ρ is the solution density. Table 1 lists uncertainty in all measurements.

Table 1: Variable uncertainties

Variable	Uncertainty
Pressure	0.5%
Density (kg/m^3)	5 kg/m^3
Absorption rate	5%
Solution flow rate	0.2%
Temperature	0.3 °C

Initially, the water vapor pressure was increased while other test parameters were held constant. Figure 4a shows the effect of water vapor pressure on the absorption rate. The results clearly show that increasing the water vapor pressure (*Pv*) linearly increases the absorption rate. The variation of the solution water vapor pressure (*Ps,w*) on the absorption rate was tested, the solution water pressure was changed while the vapor pressure was held constant. Solution water pressure varies with the solution temperature and concentration. The change in the solution pressure was achieved by varying the solution channel wall temperature from 25 to 35 °C in 2.5 °C increments. All other conditions were held constant. As indicated in Figure 4b, there is a linear decrease in absorption rate with an increase in solution temperature, which increases the solution water vapor pressure. All absorption rates given Figures 4a and 4b are normalized with respect to the pressure potential (*Pv-Ps*) and are plotted in Figure 4c. The solution water pressure used in the calculation is the average of the absorber inlet and exit. The results are consistent with an absorption rate that linearly increases with the pressure potential regardless of the source of pressure change.

Figures 4a and 4b give numerical results where experimental data agree within 15%. This difference between the numerical and experimental results can be attributed to uncertainty in the film thickness, potential inaccuracy in the solution water vapor pressure correlations used in numerical simulations, and non-uniform wall temperature in the experiment.

The validated numerical model given above was used to analyze the impact of chaotic advection on absorption characteristics of a thick absorbent flow constrained by a membrane. Table 2, below, lists input parameters of the model. The temperature of the channel bottom wall, the 3D structured heat exchanging surface, was set to vary linearly from 27.5 °C at the solution outlet to 32.5 °C at the solution inlet, to mimic a counter flow heat exchanger configuration.

Table 2: Input parameters of the numerical model

Parameter	Value
Vapor saturation temperature, T_v	5 °C
Inlet solution temperature, T_i	32.5 °C
Inlet solution concentration, C_i	60%
Solution mean velocity, u	0.05 m/s
Membrane porosity, ε	60%
Membrane pore diameter, d_m	1 μm
Tortuosity, τ	1.0
Membrane thickness, δ_m	20 μm
Absorbent channel height, CH	500 μm
Channel length, L	600 mm

Figure 5a provides the concentration contours within the flow channel. A scale factor of 0.005 is used in the x direction to show the entire flow domain. The absorbate, water vapor, is absorbed into the absorbent (LiBr solution) at the membrane-absorbent interface, the vapor-exchanging surface. As the solution flows through the channel, the thickness of the concentration boundary layer formed at that interface increases. The boundary layer acts as a resistance to mass transfer between the interface and the bulk of the solution. The results clearly suggest that most of the solution is not involved in the absorption process and leaves the channel at a high concentration.

Variations between the bulk and interface concentrations along the channel are plotted in Figure 6. At the channel inlet, a high solution concentration, with its low water vapor pressure in the solution phase, results in rapid absorption of the water vapor into the solution. This high absorption rate results in a sharp decline in the solution concentration at the interface. However, due to the low diffusion rate of the water molecules through the solution, this change is not reflected within the bulk flow. While the interface concentration decreases by 6.2 %, from 60 % to 53.8 %, over the 600 *mm* length of the channel, the average bulk concentration decreases by only 1.2 %, from 60 % to 58.8 %, over that length.

Figure 5b depicts temperature distribution within the flow. The results show a sudden increase in temperature of the interface at the channel inlet due to the release of heat at a high absorption rate where the solution is at its highest concentration. The high absorption rate causes a sizeable increase in the bulk temperature at the channel inlet. However, the relatively high heat diffusion rate in the LiBr solution results in rapid cooling of the interface. Thereafter, both the interface and the bulk temperatures closely follow the heat exchanging, cooling, surface temperature. Comparisons of the interface and bulk values of the temperature and concentration profiles indicate that the absorption process is mass-transfer limited.

Figure 7 shows a plot of the water vapor absorption into the solution film. The highest absorption rate is indicated at the channel inlet where the most highly concentrated solution is present. The absorption rate thereafter declines as the concentration boundary layer near the vapor-solution interface grows. The average absorption rate over the entire channel length is 0.0016 kg/m^2s, as indicated in Figure 4c.

The heat and mass transfer process of the base case is diffusion dominated, since the flow is laminar (R_e = 7). The diffusion limitations are overcome by incorporation of staggered herringbone structures, hereafter called “ridges”, on the heat exchanging flow channel bottom wall. The ridges generate anisotropic resistance to the absorbent flow, which stretches and twists a portion of the absorbent flow volume. A parametric study is conducted to determine the optimal ridge geometry for a membrane-based absorber. Table 3, below, provides the list of variables and their range used in the numerical simulations. The variables RH, CH, S, α, P and J are the ridge height, channel height, distance between the ridges in the x-direction, ridge angle with respect to the x-axis, ridge length in the y-direction, and the absorption rate, respectively. The simulation results discourage a 3D-surface comprised of relatively shallow ridges, for example, 100-μm in depth with RH/CH = 0.2, as that surfaces impact on the absorption rate is small. The results recommend ridges of a few hundred microns in depth to induce surface vortices with sufficient momentum to impact the main flow and continuously replenish the interface at the vapor-exchanging surface with a concentrated solution. Comparison of the absorption rates with a RH of 100, 300, and 500 μm shows that the absorption rate increases proportionally to the ridges depth. However, current scalable and economical micro-manufacturing technologies are limited for the production of deep ridges. For example, the wet etching process utilized for these experiments do not permit a depth to width ratio of more than one, and a ridge height of 300 μm was selected. Simulated geometries indicate that the maximum performance is achieved at α = 30°, S = 600 *μm*, and P = 660 *μm*. Simulation indicates that ridges having long and short arms alternated after approximately 40 ridges, as shown in Figure 8, produce high absorption rates.

Table 3: Effect of the ridge geometry on the absorption rate

RH (μm)	RH/CH	S (μm)	α (°)	P (μm)	J×10^3 (kg m^{-2}s^{-1})
100	0.2	500	45	500	2
300	0.6	500	45	500	3.4
500	1	500	45	500	3.7
300	0.6	600	45	500	3.5
300	0.6	800	45	500	3.4
300	0.6	600	30	500	3.7
300	0.6	600	15	500	3.1
300	0.6	600	30	660	4
300	0.6	600	30	1320	3

Figure 9 illustrates how the surface induced vortices control the concentration distribution within the flowing fluid. At any given cross-section, two vortices are formed, one on each arm of the ridge. The concentration contours indicate that low concentration solution at the vapor-exchanging surface is advected downward towards the bottom of the channel to the heat-exchanging surface by the transverse velocity generated by the vortices. Switching between the ridges, as shown in Figure 8, reorganizes the vortices across the cross-section to mix more dilute solution with more concentrated solution at the center of the larger vortex. The concentration contours at different cross-sections of the flow channel is illustrated in Figure 9 for this process.

Figure 10 shows the y and z components of the velocity vector along the microchannel at y = 180 *μm* and z = 750 *μm*, which is 50 *μm* below the vapor-exchanging surface. The results show a major difference of approximately 4- to 5-fold between the y component of the velocity on the long and short ridges. The maximum transverse velocity in the y direction occurs on the long arm of the ridges and the average value of the y-velocity is 1.4 *mm/s*, which is 12 % of the x component of the velocity.

Figure 11a illustrate the concentration contours at y = 180 *μm* cross section. The results clearly illustrate how ridges substantially change the concentration distribution in the absorbent film. The solution is well mixed such that mass transfer inside the flow channel is not dominated by molecular diffusion. The surface induced vortices take absorbent from the bulk solution to the vapor-liquid interface and continuously disturb the concentration boundary layer growth as the absorbed water molecules are advected from the vapor-exchange surface to maintain a high solution concentration at the vapor-exchange surface.

The temperature contours, shown in Figure 11b, indicate that the advection process significantly impacts the temperature gradient. The mixing of the warm solution from the vapor-exchange surface with the relatively cool bulk solution distributes the interface heat throughout the bulk. However, because the diffusive heat transport from the heat-exchanging surface is significant, exceeding the advective heat transport, a thermal gradient in the z-direction is established and maintained.

The role of mixing in the absorption process is indicated by variations of the interface and bulk values of the concentration and temperature, as plotted in Figure 12. In contrast to the base case, illustrated in Figure 5, the bulk concentration, X_{bulk}, more closely resembles the interface concentration, $X_{interface}$, with about a 2% difference throughout the entire channel length. A significant fluctuation, of about 0.5 %, is observed in the interface concentration. The mixing process involves two vortices forming over the long and short arms of the ridges, which is responsible for the smaller variation in bulk and vapor-exchange interface concentrations and temperatures. The difference in the strength of the two vortices is highlighted in Figure 10, where the y component of velocity on the long arm of the ridge is seen to be 4 to 5 times larger than y component of velocity over the short arm of the ridges. Reduction in the y component of the velocity, at x = 30 *mm*, slows the interface replenishment process, resulting in a decrease in the vapor-exchange interface concentration which increases again when the solution flows over the long arms of the ridges, at x = 60 *mm*. This structuring also produces fluctuation of the interface temperature.

Figure 13 plots absorption rates along a channel's length. As in the base case, shown in Figure 7, the high absorption rate at the channel inlet quickly declines within a short distance from the inlet for the 3D-structured channels; however, the rate of decline is significantly less than that of the base case. The absorption rate stabilizes at a much higher rate than that of the base case due to the fact that the modified fluid flow replenishes the vapor-exchange surface with a concentrated solution. This absorption rate fluctuates. At each fluctuation, the absorption rate reaches a maximum within a short flow distance, after which the absorption rate declines. By switching between the position of the short and long arms of the ridge, in the manner indicated in Figure 8, the absorption rate again increases. Alternating between the two surface patterns continuously brings the concentrated solution from the middle of the vortices to the vapor-liquid interface, as indicated in Figure 9. This alternation is critical to maintaining a high absorption rate. If this alternation does not take place, the absorption rate continuously declines. Overall, the process results in an average absorption rate of 0.004 kg/m^2s, which is approximately 2.5 times higher than the absorption rate achieved in the base case, as is indicated in Figure 4c.

The enhancement in the absorption rate proportionally increases the heat release at the vapor-exchange interface. These results also indicate a significant fluctuation in the interface temperature. The amplitude of these fluctuations increases as the difference between the solution temperature at the vapor-exchange surface and at the heat-exchange, cooling, surface increases along the channel.

Implementation of the surface vortices enhances absorption rates. This increase in the absorption rate resulted in significant heating of the solution and increased the difference between the vapor-exchange surface and the heat-exchange surface. To better cool the solution, the sides of the channel are thermally conductive walls. In addition to impacting the heat transfer field, the thermally conductive side walls facilitate membrane assembly over the flow channels, as illustrated in Figure 3. Figure 14 plots the temperature and concentration profiles for channels with thermally conductive side walls, where the average temperature difference between the vapor-exchanging surface and the heat-exchanging surface reduces to 1.27 °C, from 3.45 °C when there are no thermally conductive side walls. However, inclusion of side walls weakens the strength of the vortices, as evidenced by the decrease in the y component of the velocity, as indicated in Figure 10. The difference between the concentrations at the interface and bulk, as shown in Figure 14, with the difference where no sidewalls are present, as plotted in Figure 12, indicate that by adding sidewalls the concentration difference increases from 3.25 % to 4.3 %. Hence, although adding sidewalls reduces heat transfer resistance, the addition slightly increases mass transfer resistance. The overall impact of adding the sidewalls to the absorption rate is indicated in Figure 13. A decline in the absorption rate occurs at the beginning of the channel with inclusion of sidewalls, which can be attributed to a reduction in the transverse velocity. However, due to a significant improvement is the solution cooling process; a higher absorption rate is achieved over the latter portion of the channel's length. Overall, adding thermally conductive sidewalls results in a small improvement of the absorption rate to 0.0042 kg/m^2s.

A schematic of an exemplary desorber according to an embodiment of the invention is shown in Figure 15. The overall size of the desorber is 16.8 × 16.5 cm^2. The ridges of the 3D-structured surface were machined on a corrosion-resistant C-22 Hastelloy over a 5.7 × 8.9 cm^2 area. A hydrophobic nanofibrous membrane was placed on the solution microchannels and secured in place by a perforated stainless steel sheet. This arrangement forms 200±10 μm deep solution channels, which was verified by comparison of the solution pressure drop with that predicted by laminar flow theory. Twelve thermocouples were installed within three trenches machined on the backside of the Hastelloy plate to measure wall temperatures. The remaining space within the trenches was filled with a high temperature conductive epoxy. A flexible thin-film heater (Omega Engineering, CT) was assembled over the entire surface to define the heat-exchange surface.

A micro gear pump (HNP Mikrosysteme, Germany) was attached to the desorber to drive the dilute LiBr solution through a heat exchanger, where the solution is preheated to a desired temperature before entering the desorber. The desorbed water vapor flows to a condenser, and the concentrated LiBr solution leaves the desorber and enters a Coriolis mass flow meter (Bronkhorst USA), where the LiBr solution flow rate and concentration are evaluated. The condensed water from the condenser flows through a Coriolis mass flow meter (Micro Motion, Inc.), where the desorption rate is directly measured. Three pressure transducers with a range of 0-100 kPa were installed to monitor desorber pressure conditions. Two of the transducers measure the LiBr solution flow pressure at the desorber inlet and outlet. The average solution pressure (Ps) was calculated from the readings of these transducers. The third transducer measured the vapor pressure (Pv) at the desorber vapor exit. All tests were conducted at a solution flow rate of 2.5 kg/hr and a solution inlet temperature of 60 °C.

The numerical domain is a rectangular microchannel with a porous hydrophobic top wall and a heated bottom surface, and was treated in the manner for the absorber, above, to model the heat and mass transport within the solution. As with the absorber, the desorption process in microchannels without any surface features, a base case, was experimentally and numerically studied. Figure 16 shows the experimental desorption rates as a function of heat-exchanging surface temperature, Tw, which is the average reading of the twelve thermocouples imbedded within the heated wall.

A test was conducted using a vapor pressure, P_v, of 6 kPa, as the vapor pressure in a typical single-effect absorption refrigerant system (ARS) is between 5 to 10 kPa, depending on the condenser temperature, a solution pressure, P_s, of 23 kPa, and a solution concentration of 48 %. Solution pressure was selected to be sufficiently higher than the vapor pressure such that both modes of desorption could be realized. The first non-zero desorption rate was measured at a surface temperature of approximately 60 °C. Desorption at this temperature results from a positive driving pressure between the solution water vapor pressure, $P_{s,w}$, and the external vapor pressure, for example, $P_{s,w} - P_v > 0$. Thermodynamic properties of the LiBr solution at the desorber inlet concentration confirmed that the solution water vapor pressure exceeded 6 kPa at a solution temperature of 60 °C, as indicated in Figure 17. The desorption rate steadily increases with the heat-exchanging surface temperature, or wall temperature, at a moderate pace, since increasing the solution temperature increases the solution water vapor pressure, and, consequently, increases the driving pressure potential. The desorption rate diminishes when the vapor pressure increases to 10 kPa, due to the decrease in pressure potential.

Figure 16 provides a comparison of the numerical and experimental results. The numerical results, filled symbols, closely follow the experimental data, unfilled symbols. The small difference between the two is presumably due to uncertainty in the film thickness, inaccuracy in the solution water vapor pressure correlations used in the numerical code, and non-uniformity of the wall temperature. To probe the cause of the observed decline in the rates of increase of desorption at moderate heat-exchanging surface temperatures, as shown in Figure 16, a set of numerical simulations was conducted. The results suggested that a small variation in the solution concentration entering the desorber is responsible for the observed behavior. Although efforts were made during the tests to maintain a constant inlet concentration, the system stabilized at a slightly different concentration for each test, which resulted in a gradual increase in the solution inlet concentration from 48 % to 51 % within a heat-exchanging surface temperature range of 60 °C to 83 °C.

At a solution pressure of 23 kPa, when the heat exchange surface temperature was increased a few degrees above the solution saturation temperature, about 93 °C at the average solution concentration of 52 %, as indicted in Figure 17, the desorption rate rose significantly, as indicated in Figure 16, which signifies a change in the desorption regime. This change is associated with fluctuations in the desorption rate, solution flow rate, and pressure readings due to instabilities associated with boiling the solution flow. In a subsequent test, the solution pressure was increased to 30 kPa to suppress boiling by increasing the solution saturation temperature (to about 103 °C at an average concentration of 53 %, as indicated in Figure 17, while other test conditions were maintained. The results shown in Figure 16 display a lower desorption rate when boiling is suppressed. Figure 18 provides a numerical depiction of the LiBr concentration distribution at the solution pressure of 30 kPa with an inlet concentration of 52 %. This figure highlights that a significant portion of the solution does not participate in the desorption process due to the slow water molecules diffusion rate. A comparison of the numerical base case and the experimental desorption rates are also provided in Figure 16.

To continuously force water-rich solution to the vapor-exchanging surface in contact with the membrane, the 3D-structured ridges were constructed on the heat-exchanging surface on the bottom wall of the flow channel, as illustrated in Figure 19i. As with the absorber, it was determined by numerical simulation that the most important design factor for the desorber's 3D-structured surface is the ridge depth to channel height ratio. The results presented here are for a depth to height ratio of one. Figure 19i provides details of the design implemented in the numerical simulation. In Figure 19ii, two pathlines in the solution microfilm are traced to illustrate the generation of transverse currents within the flow stream.

Fig. 20i shows a 3D view of the concentration contours depicting the impact of vortices on the concentration field. The numerical simulation was conducted at a solution pressure of 30 kPa, a vapor pressure of 10 kPa, an inlet concentration of 52 %, and a heat-exchanging surface wall temperature of 103 °C. The replenishment of the concentrated solution at the membrane-solution interface with the water-rich solution is indicated by the concentration contours at different cross sections, as shown in Figure 20ii. The cross sections are chosen between x = 0 mm and x = 29 mm. At x = 0 mm, the bulk solution concentration is 52 %. As the solution flows along the microchannel, the vortices force the concentrated solution at the vapor-exchange surface near the membrane downward, as indicated at x = 6 to 14 mm. That volume of concentrated solution is replaced with the water-rich dilute solution that rises from the heat-exchanging surface at the bottom of the flow channel, as indicated at x = 18 to 29 mm. The bulk concentration reached approximately 53.5 % at x = 29 mm.

The concentration contours at y = 1.32 mm cross-section are shown in Fig. 21. When compared to the base case of Figure 18, the introduction of ridges on the heat-exchange surface substantially modifies the concentration distribution. The transverse currents due to the 3D-structures on the heat-exchanging surface continuously interrupt the boundary layer growth, which results in a uniform concentration distribution at each cross-section. Although the mass transfer mechanism within the bulk flow has changed from diffusion to convection, the desorption process at the membrane-solution interface remains diffusion limited.

Variations of important parameters in the solution flow are plotted in Figure 22. At the desorber inlet, since the solution water vapor pressure is significantly lower than the external vapor pressure, vapor is absorbed into the solution, giving a negative desorption rate. This phenomenon results in a significant reduction in the interface concentration. However, the high heat transfer coefficient associated with the microchannel flow results in rapid heating of the solution shortly after it enters the desorber such that the solution water vapor pressure exceeds the external vapor pressure, for example, of 10 kPa, and the desorption process begins. As the water vapor desorbs from the solution, the interface and the bulk solution concentrations increase along the flow direction. The desorption rate gradually declines as the overall concentration of the solution increases along the flow channel. The average desorption rate from the solution in this case is approximately 0.0068 kg/m2s, which is about 1.7 times greater than that of the base case and is about 1.3 times higher than that of boiling at the same surface temperature.

All patents, patent applications, provisional applications, and publications referred to or cited herein are incorporated by reference in their entirety, including all figures and tables, to the extent they are not inconsistent with the explicit teachings of this specification.

It should be understood that the examples and embodiments described herein are for illustrative purposes only and that various modifications or changes in light thereof will be suggested to persons skilled in the art and are to be included within the spirit and purview of this application.

CLAIMS

We claim:

1. An absorber or desorber, comprising:

at least one micro-channel, wherein said micro-channel comprises at least one 3-D structured heat-exchanging surface;

a membrane situated distal to the 3-D structured heat-exchanging surface residing on the micro-channel; and

a solution, wherein the membrane is proximal to a vapor-exchanging surface of the solution residing within the micro-channel of the absorber or desorber.

2. The absorber or desorber according to claim 1, wherein the membrane is a nanoporous membrane.

3. The absorber or desorber according to claim 2, wherein the nanoporous membrane is hydrophobic and the solution is an aqueous solution.

4. The absorber or desorber according to claim 3, wherein the aqueous solution is a LiBr solution.

5. The absorber or desorber according to claim 1, wherein the 3-D structured heat-exchanging surface comprises a series of ridges, wherein the ridges form a herringbone structure.

6. The absorber or desorber according to claim 5, wherein the ridges have a short arm and a long arm, wherein a portion of the series of ridges have the short arms oriented to one side of the micro-channel alternate with a second portion of the series of ridges having the short arms oriented to a second side opposite the first side.

7. An absorption refrigeration systems (ARSs), comprising at least one absorber and/or at least one desorber according to claim 1.

8. A method of absorbing vapors, comprising

providing an absorber according to claim 1;

flowing a solution comprising a solvent through the micro-channels of the absorber;

cooling the 3-D structured heat-exchanging surface; and

exposing vapors of the solvent to the vapor-exchanging surface of the solution through the membrane.

9. A method of desorbing vapors, comprising

providing an desorber according to claim 1;

flowing a solution comprising a solvent through the micro-channels of the absorber;

heating the 3-D structured heat-exchanging surface; and

expelling vapors of the solvent from the vapor-exchanging surface of the solution through the membrane.

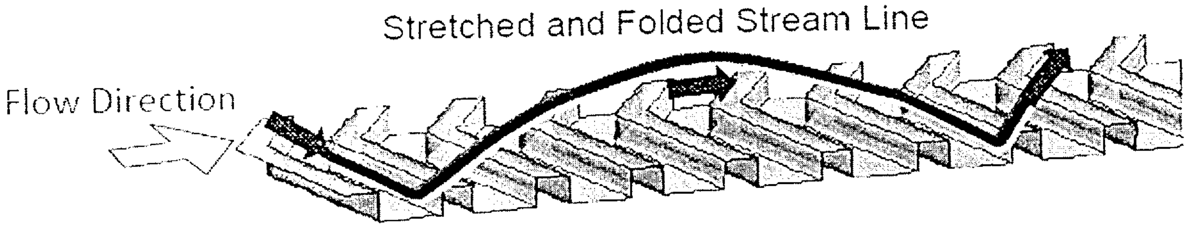

Figure 1

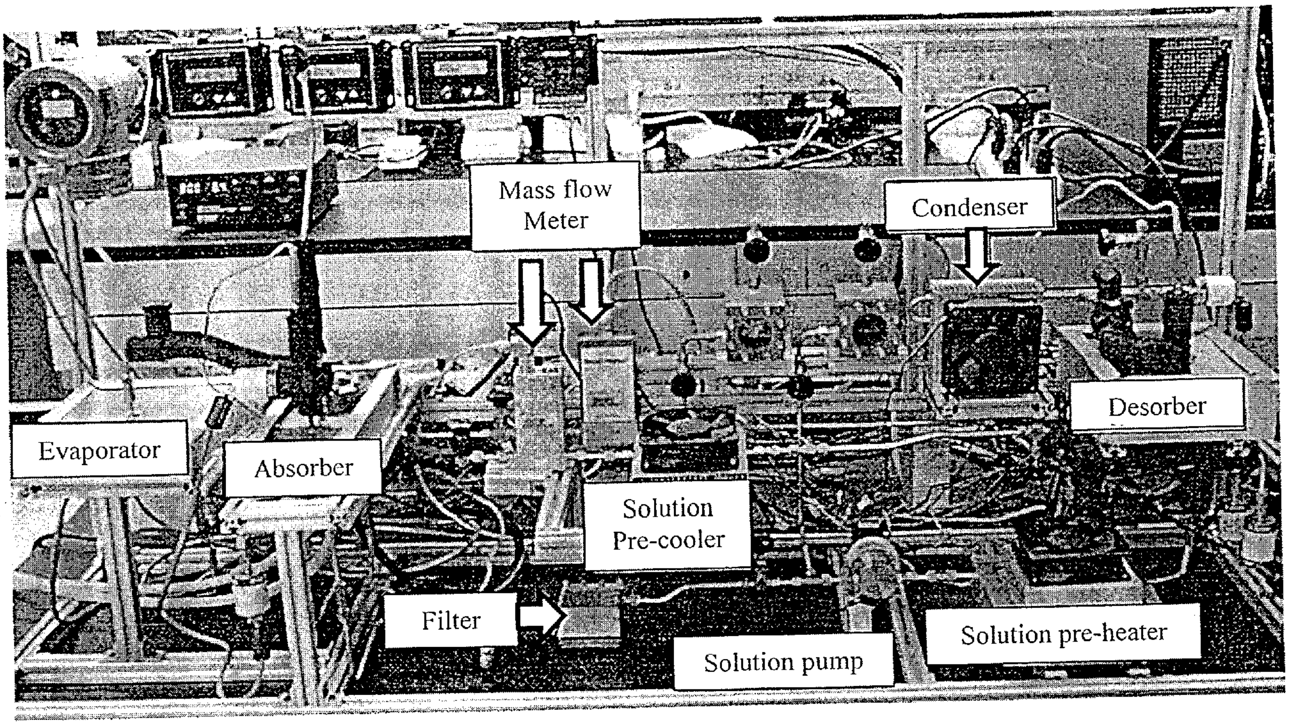

Figure 2

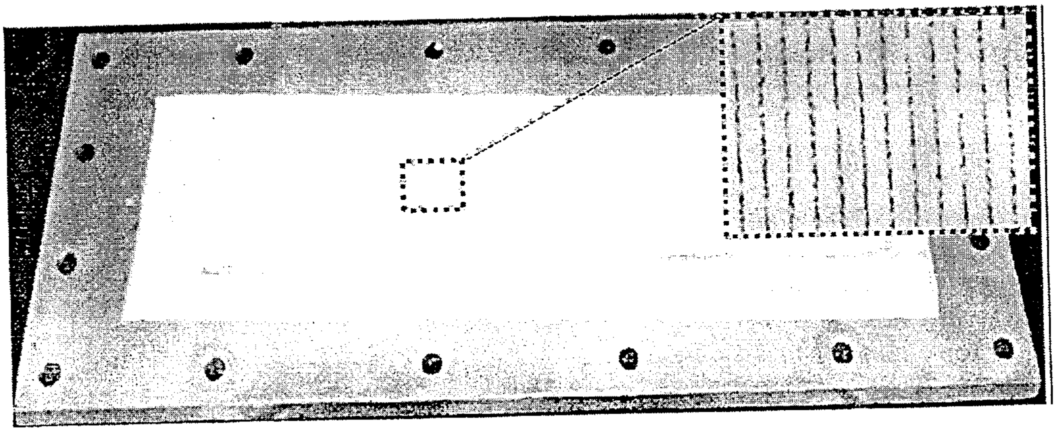

Figure 3

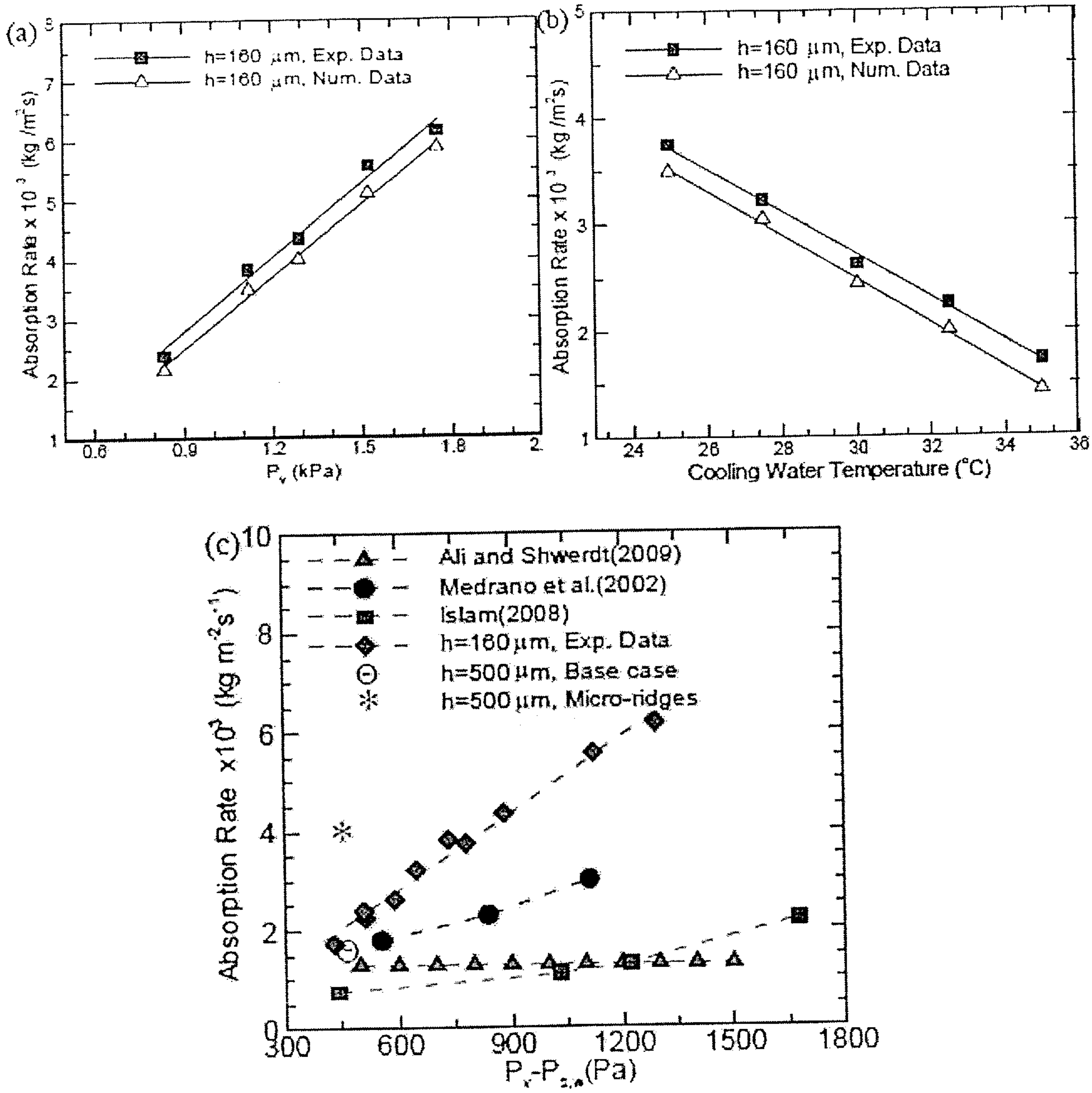
(a)
h=160 μm, Exp. Data
h=160 μm, Num. Data
Absorption Rate x 10⁻³ (kg/m²s)
1
2
3
4
5
6
7
8
0.6
0.9
1.2
1.5
1.8
2
P_v (kPa)
(b)
h=160 μm, Exp. Data
h=160 μm, Num. Data
Absorption Rate x 10⁻³ (kg/m²s)
1
2
3
4
5
24
26
28
30
32
34
36
Cooling Water Temperature (°C)
(c)
Ali and Shwerdt(2009)
Medrano et al.(2002)
Islam(2008)
h=160 μm, Exp. Data
h=500 μm, Base case
h=500 μm, Micro-ridges
Absorption Rate x10³ (kg m⁻²s⁻¹)
0
2
4
6
8
10
300
600
900
1200
1500
1800
P_v-P_{s,e}(Pa)

Figure 4

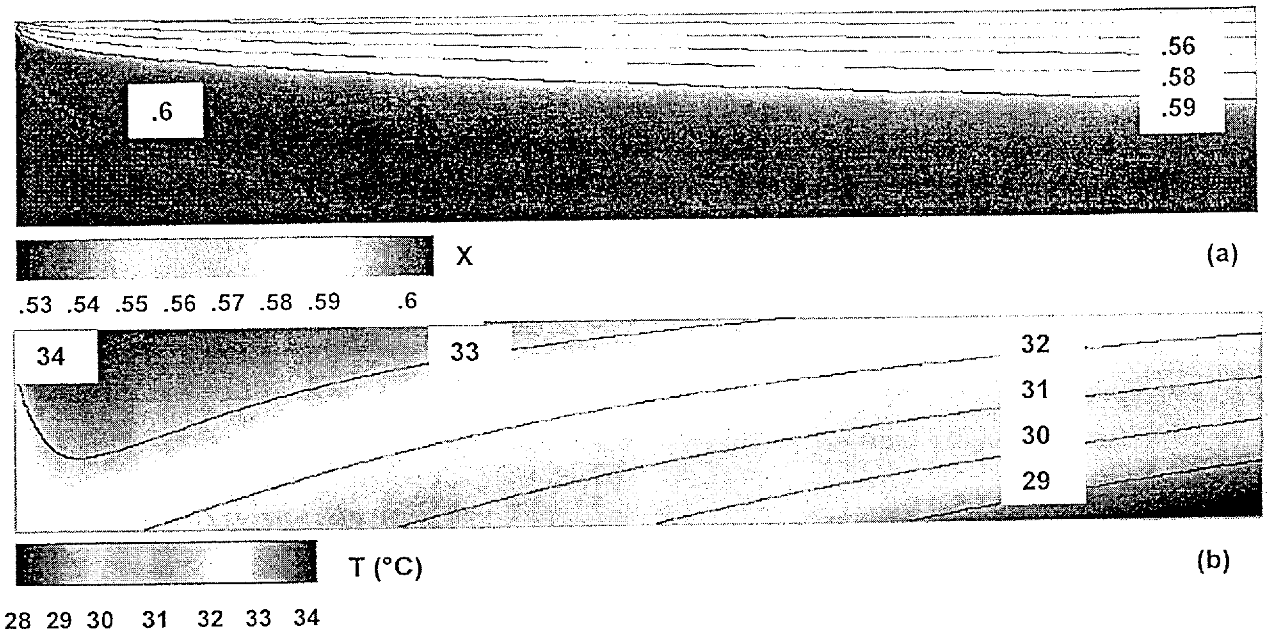

Figure 5

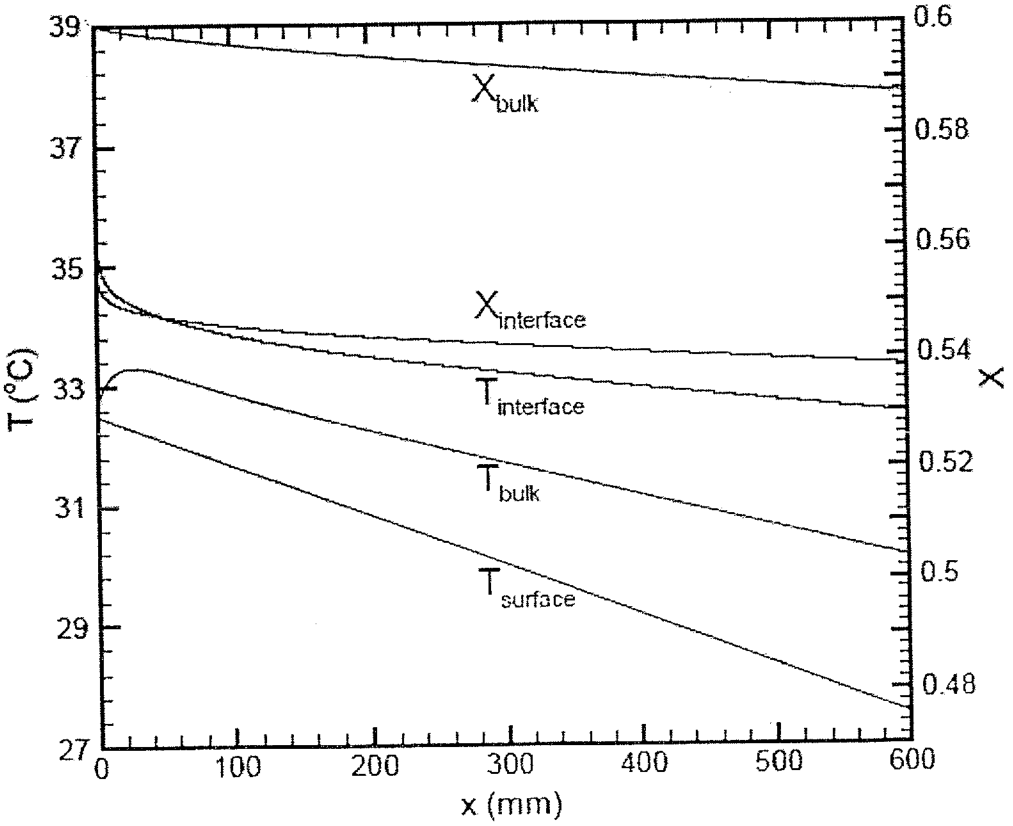

Figure 6

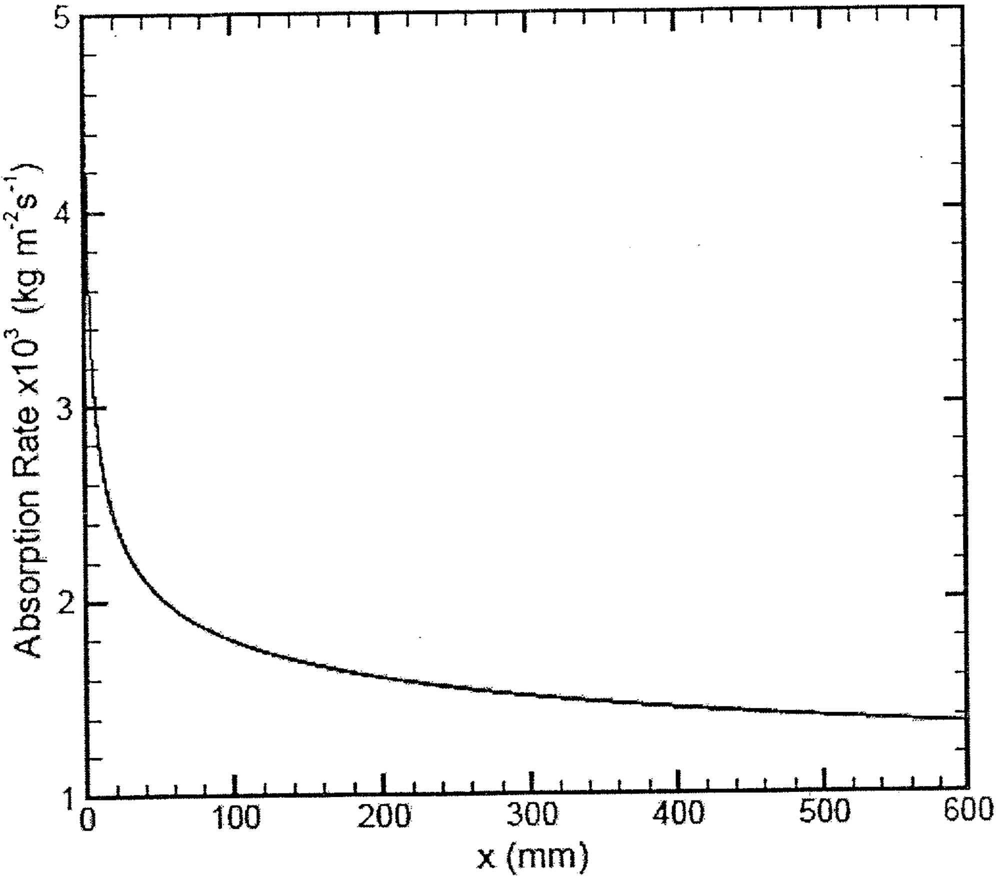

Figure 7

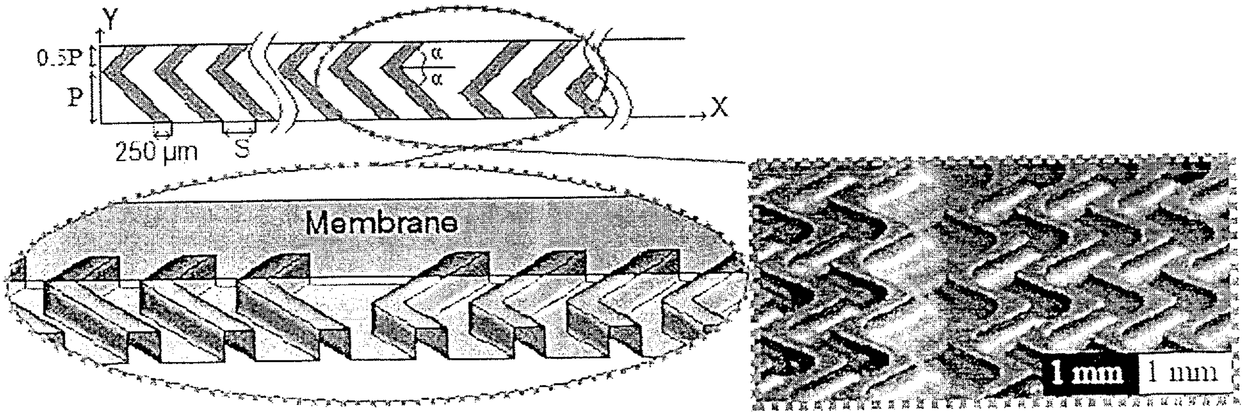

Figure 8

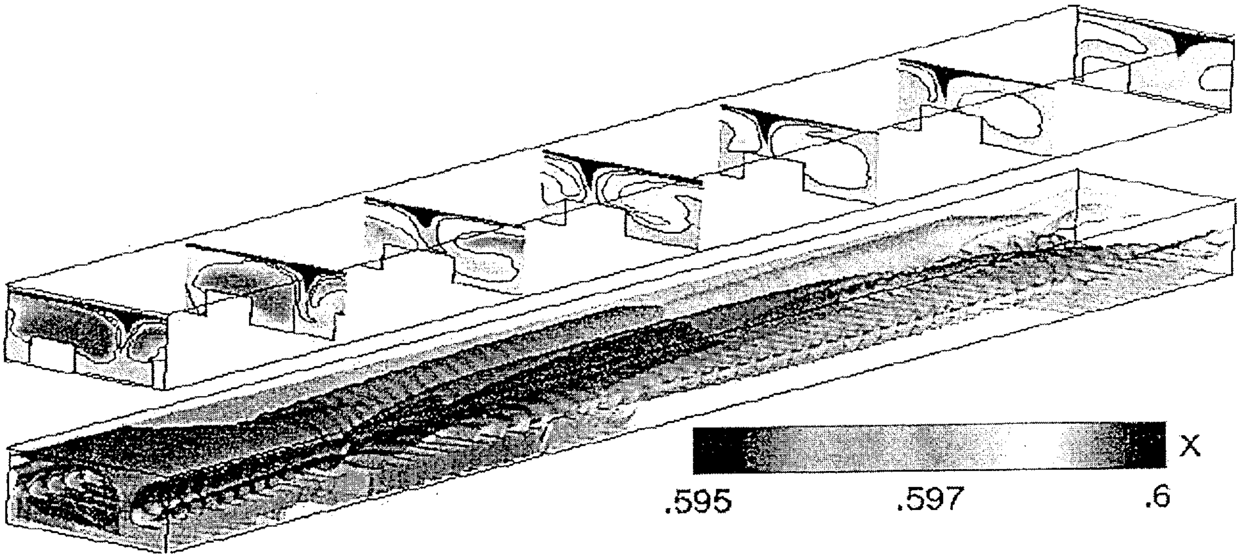

Figure 9

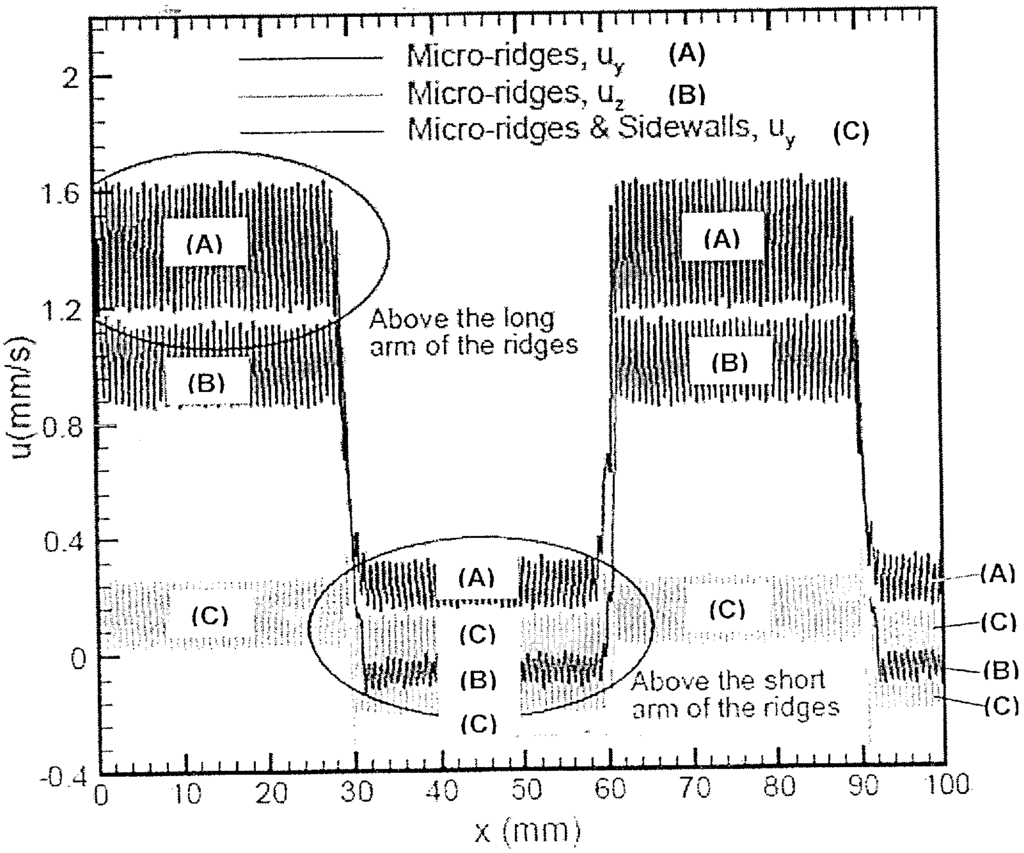

Figure 10

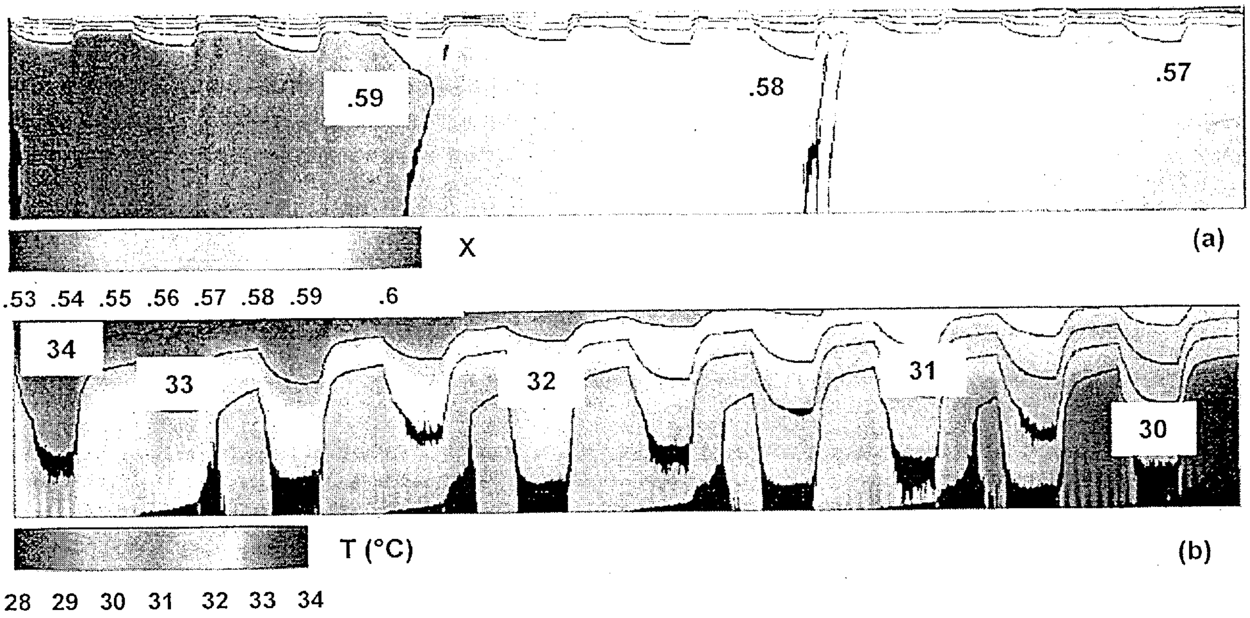

Figure 11

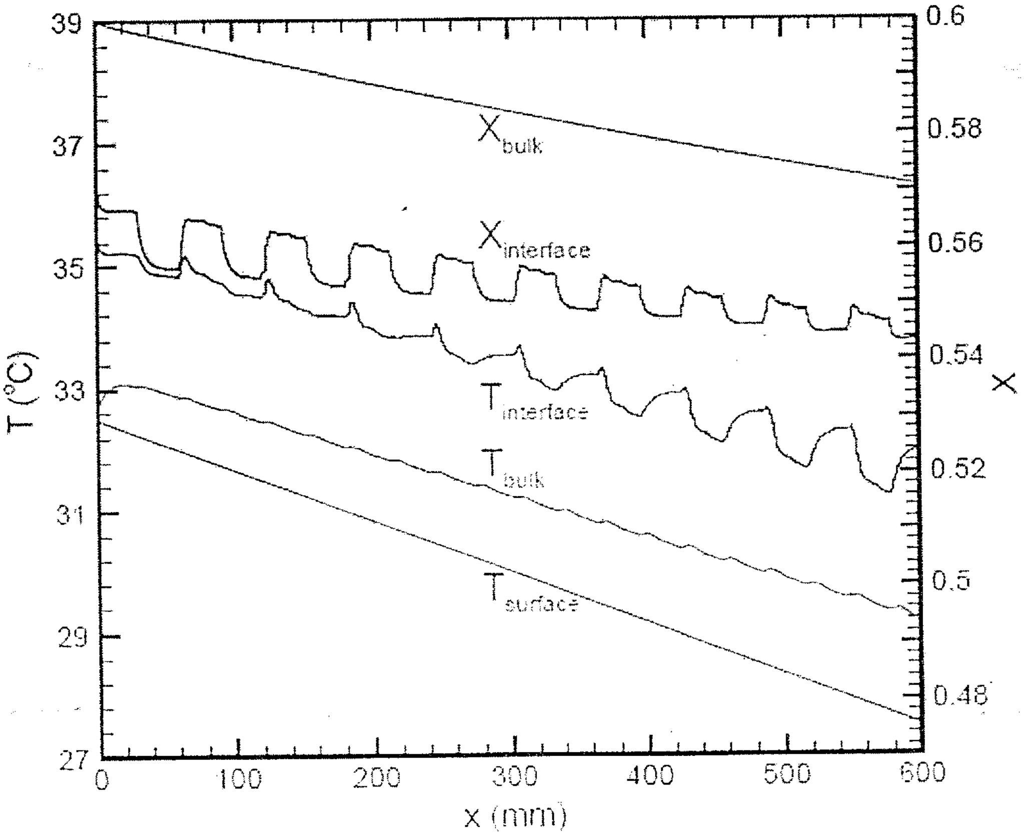

Figure 12

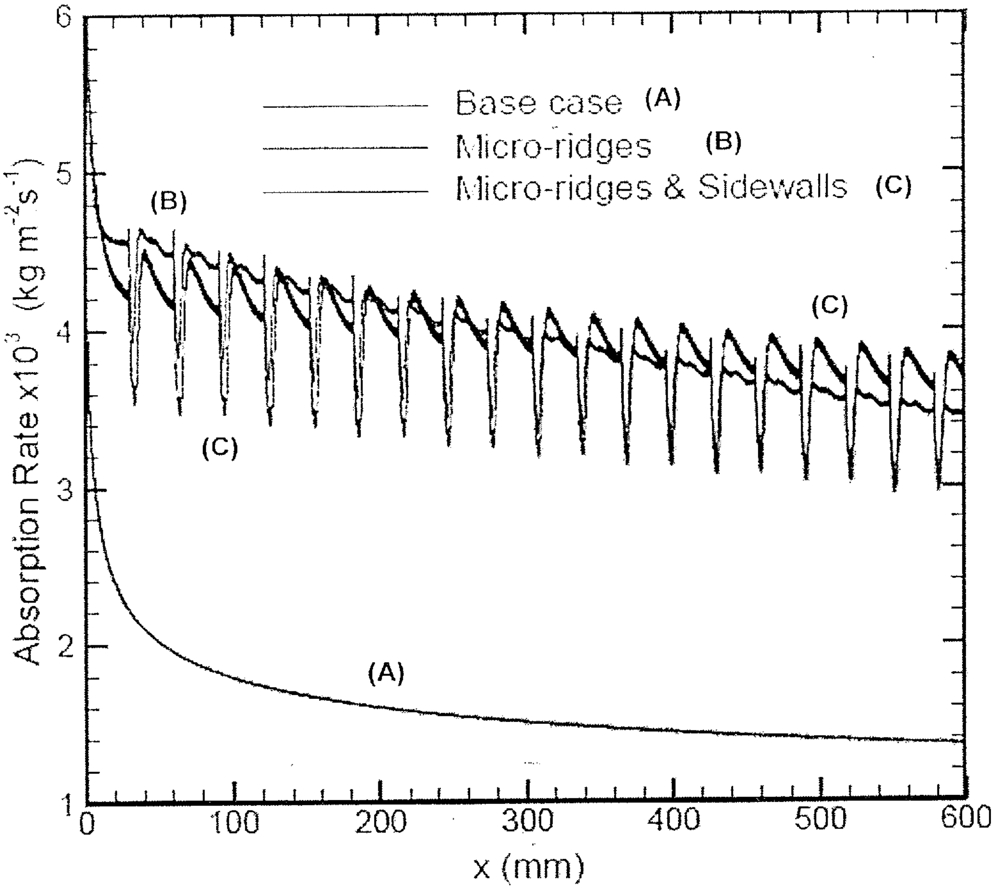
Base case (A)
Micro-ridges (B)
Micro-ridges & Sidewalls (C)
(A)
(B)
(C)
(C)
Absorption Rate x10^{3} (kg m^{-2}s^{-1})
x (mm)
1
2
3
4
5
6
0
100
200
300
400
500
600

Figure 13

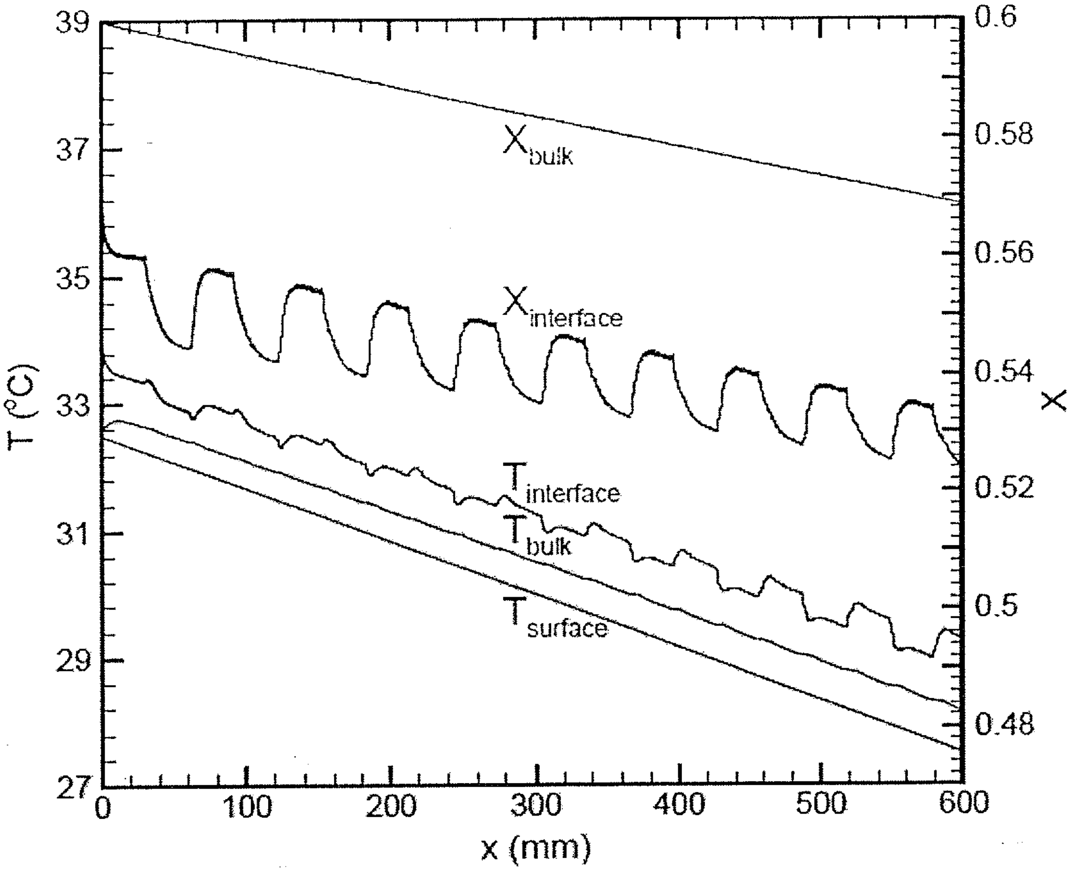

Figure 14

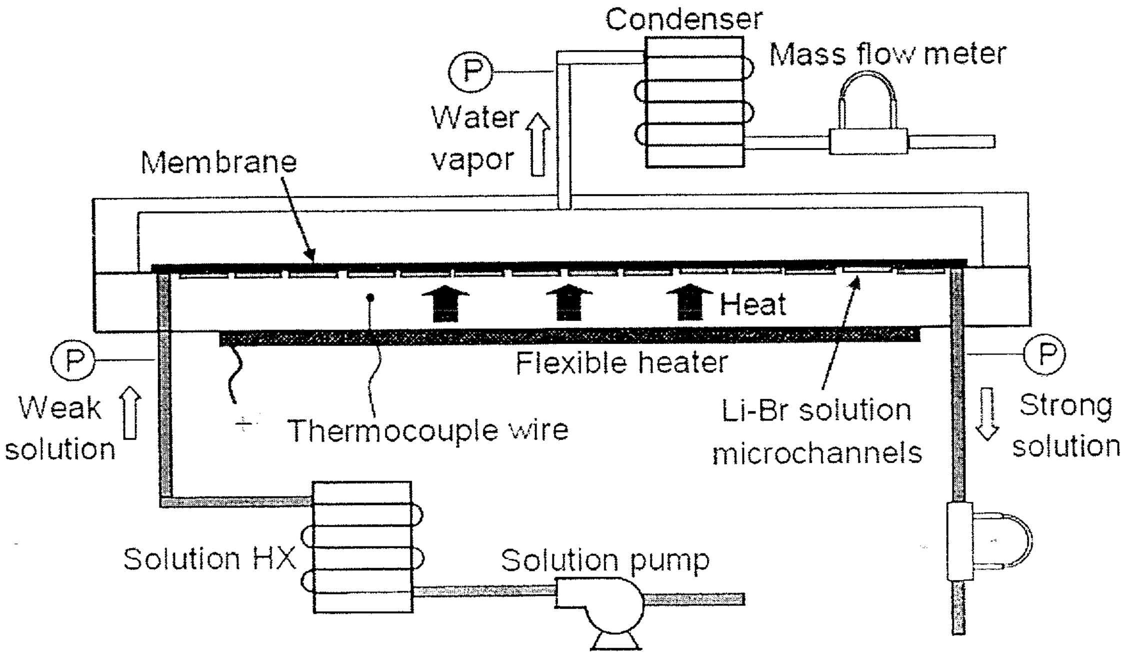

Figure 15

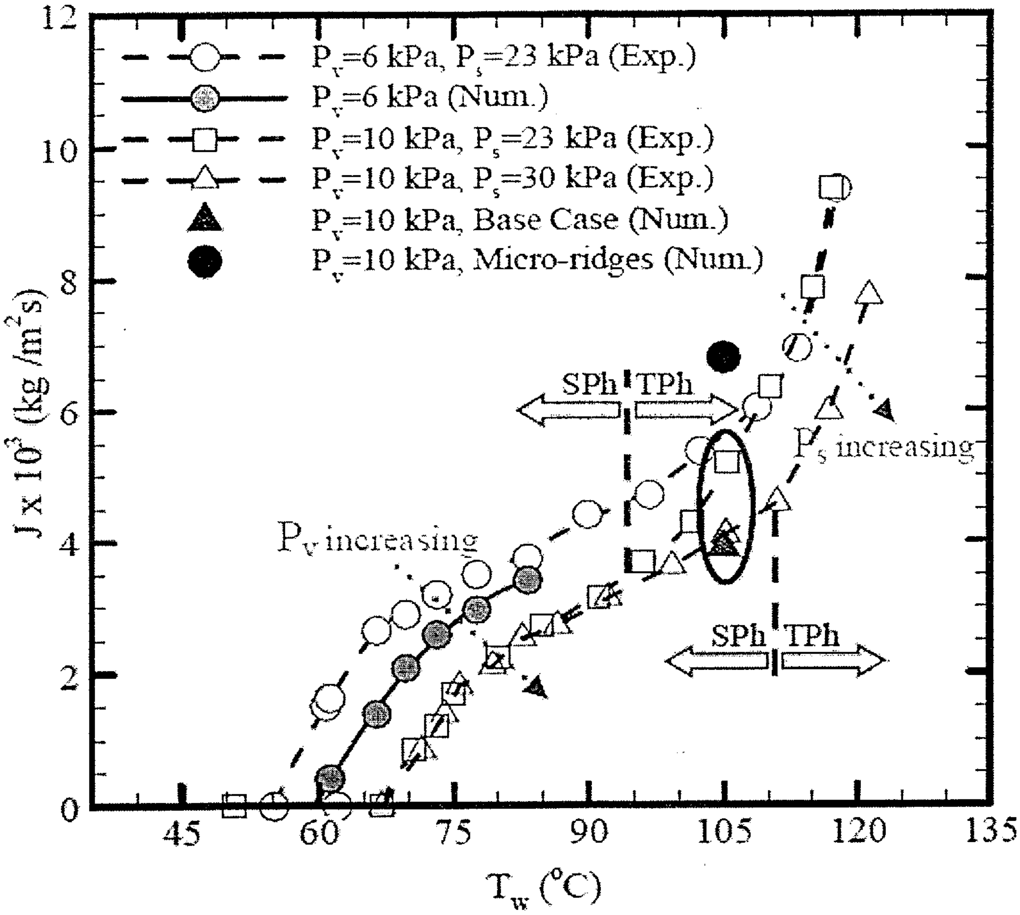
P_v=6 kPa, P_s=23 kPa (Exp.)
P_v=6 kPa (Num.)
P_v=10 kPa, P_s=23 kPa (Exp.)
P_v=10 kPa, P_s=30 kPa (Exp.)
P_v=10 kPa, Base Case (Num.)
P_v=10 kPa, Micro-ridges (Num.)
SPh
TPh
SPh
TPh
P_v increasing
P_s increasing
$J \times 10^3$ (kg /m^{2}s)
0
2
4
6
8
10
12
45
60
75
90
105
120
135
T_w (°C)

Figure 16

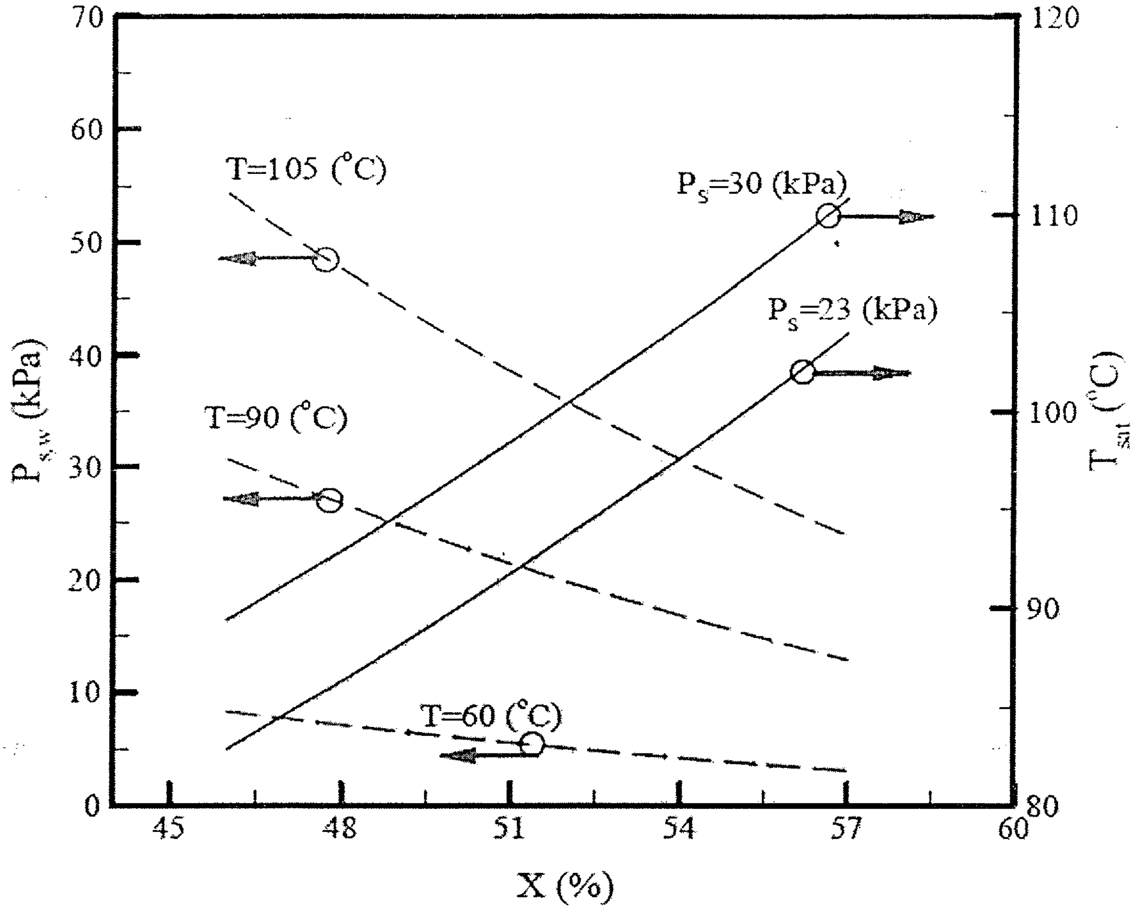

Figure 17

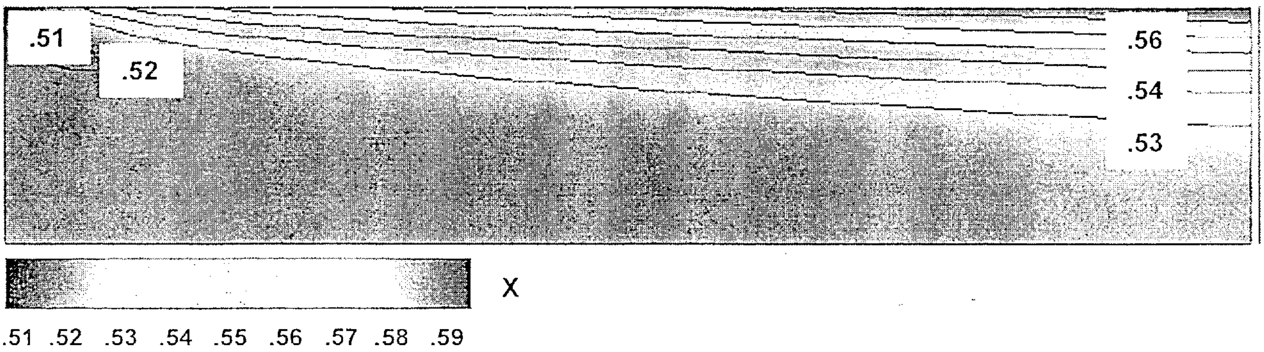

Figure 18

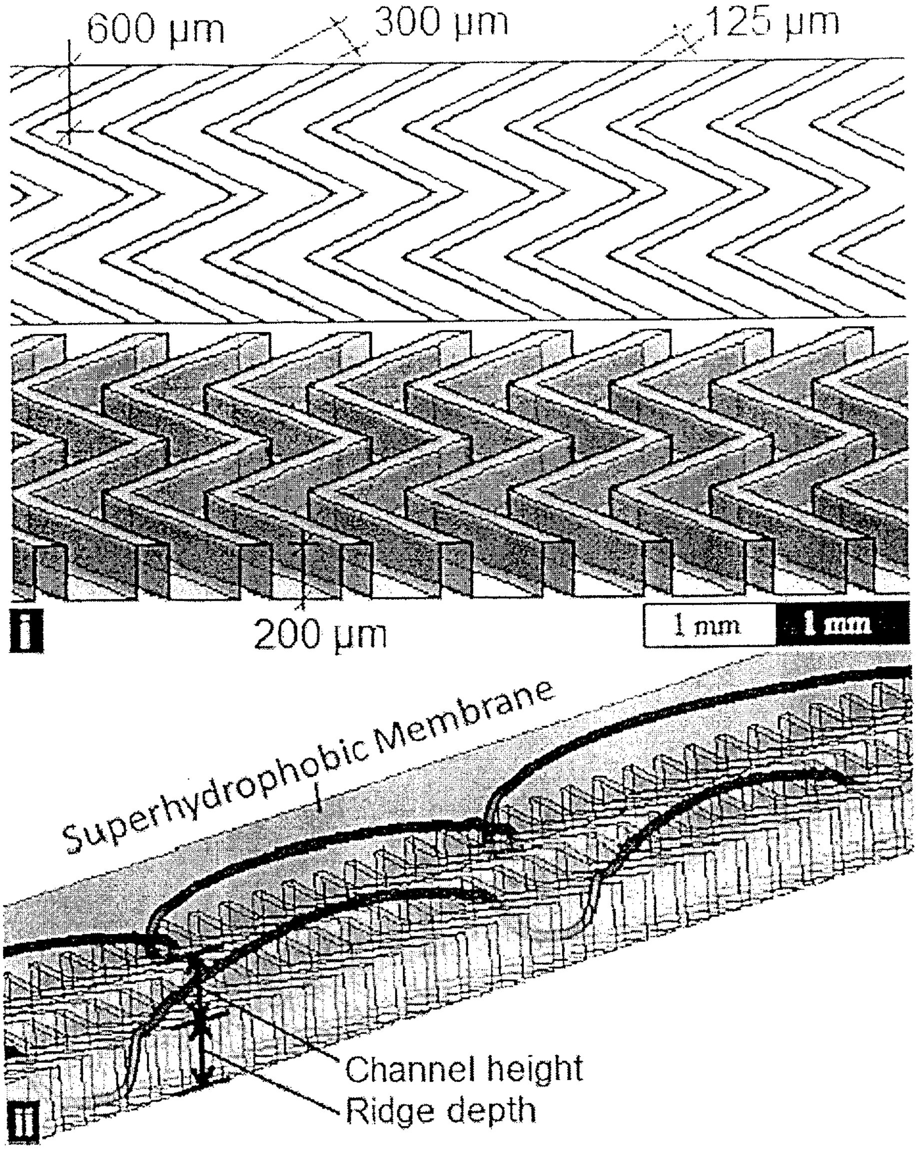
600 µm
300 µm
125 µm
i
200 µm
1 mm
1 mm
Superhydrophobic Membrane
Channel height
Ridge depth
ii

Figure 19

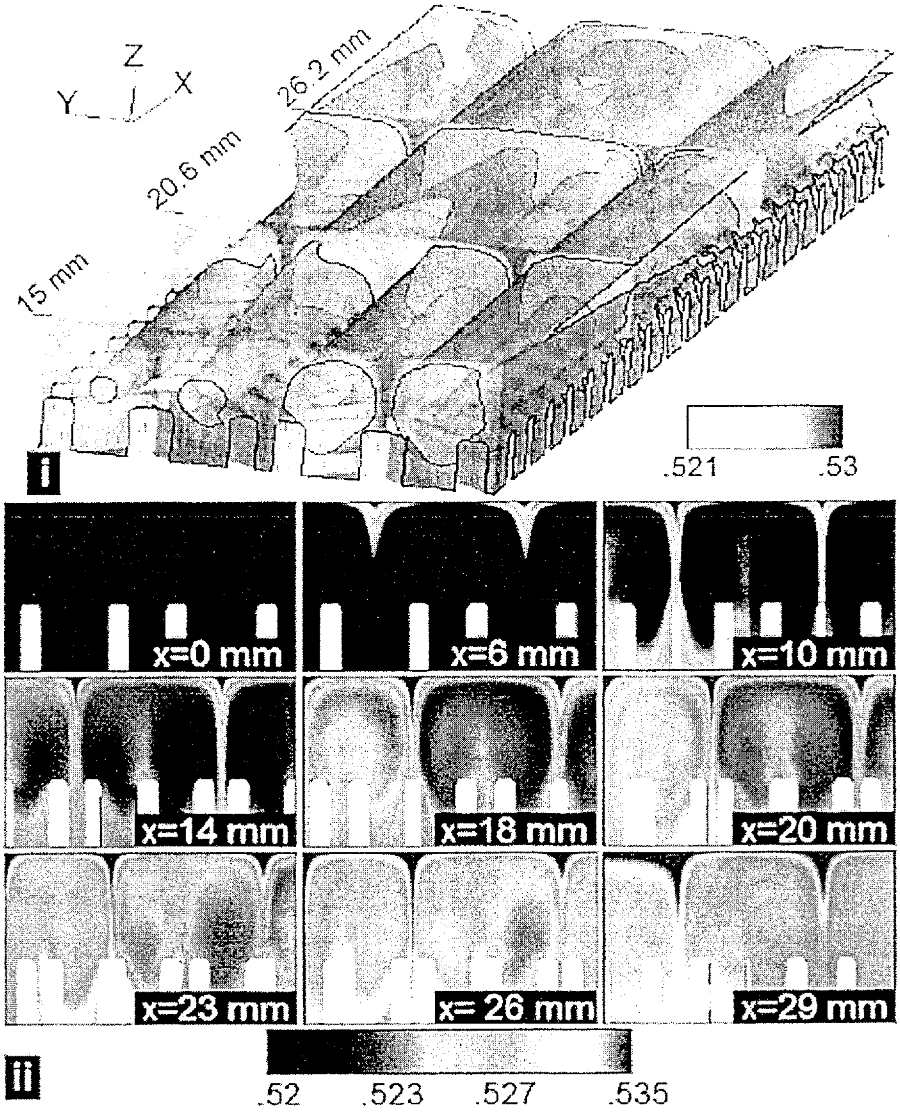

Figure 20

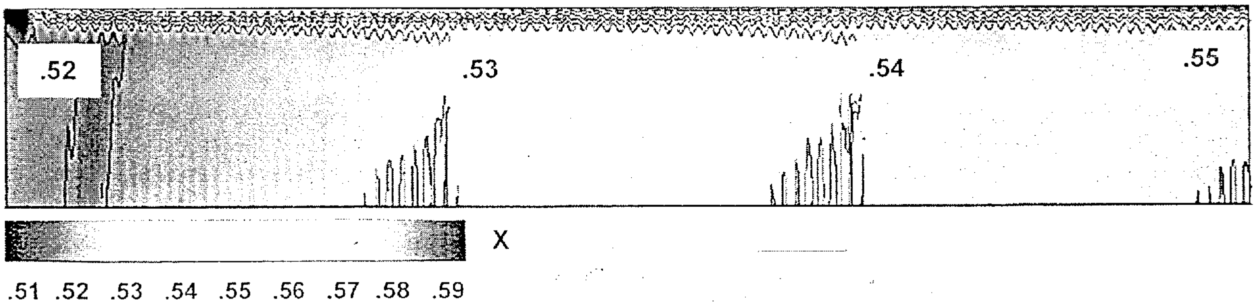

Figure 21

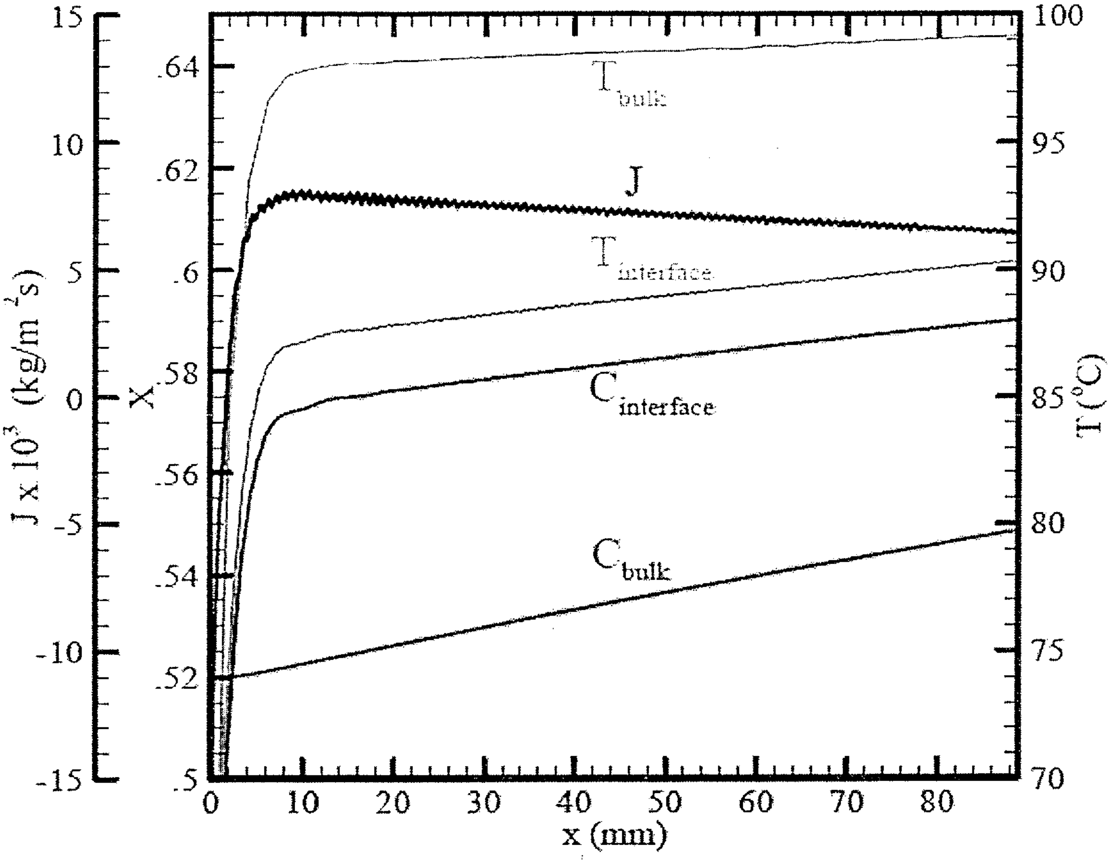
T_{bulk}
J
$T_{interface}$
$C_{interface}$
C_{bulk}
J x 10^3 (kg/m^{2}s)
X
T (°C)
x (mm)
15
10
5
0
-5
-10
-15
.64
.62
.6
.58
.56
.54
.52
.5
100
95
90
85
80
75
70
0
10
20
30
40
50
60
70
80

Figure 22

INTERNATIONAL SEARCH REPORT

International application No.
PCT/US14/72664

A. CLASSIFICATION OF SUBJECT MATTER

IPC(8) - F25B 15/06, 15/16, 17/00 (2015.01)
CPC - B01F 5/0655, 2005/0621, 2005/0623
According to International Patent Classification (IPC) or to both national classification and IPC

B. FIELDS SEARCHED

Minimum documentation searched (classification system followed by classification symbols)

IPC(8): B01D 53/14; B01F 5/06; B81B 1/00; F25B 15/00, 15/06, 15/16; 17/00, 35/02 (2015.01); CPC: B01D 53/14, 53/1425; B01F 5/0602, 5/0607, 2005/0621, 2005/0623, 5/0655; F25B 15/00, 15/06, 15/16, 27/007, 35/02, 2315/002; Y02B30/62

Documentation searched other than minimum documentation to the extent that such documents are included in the fields searched

Electronic data base consulted during the international search (name of data base and, where practicable, search terms used)

PatSeer (US, EP, WO, JP, DE, GB, CN, FR, KR, ES, AU, IN, CA, INPADOC Data); Google; Google Scholar; ProQuest; IP.com; absorb, chevron, desorb, diffuse, exchange, gas, heat, herringbone, LiBr, liquid, membrane, microchannel, microfeature, microfluidic, micropattern, nanomembrane, pattern, permeable, refrigerant, ridges, rough, transport, V-shape, vapor, vortices

C. DOCUMENTS CONSIDERED TO BE RELEVANT

Category*	Citation of document, with indication, where appropriate, of the relevant passages	Relevant to claim No.
X --- Y	WO 2013/063210 A1 (UNIVERSITY OF FLORIDA RESEARCH FOUNDATION, INC.) 02 May 2013; abstract; page 3, lines 2-3; page 3, lines 14-21; page 4, lines 5-11; page 4, lines 24-32; page 5, lines 5-19; page 5, line 20--page 6, line 5; figures 7, 8	1-4, 7-9 ---------- 5-6
Y	US 2007/0017633 A1 (TONKOVICH, AL et al.) 25 January 2007; figure 3b; paragraphs [0054], [0058], [0108]-[0109], [0142], [0156]	5-6
A	US 2004/0262223 A1 (STROOK, AD et al.) 30 December 2004; entire document	1-9
A	US 2007/0263485 A1 (YANG, J-T et al.) 15 November 2007; entire document	1-9
A	US 2005/0286227 A1 (ERTURK, H et al.) 29 December 2005; entire document	1-9

☐ Further documents are listed in the continuation of Box C. ☐ See patent family annex.

* Special categories of cited documents:
"A" document defining the general state of the art which is not considered to be of particular relevance
"E" earlier application or patent but published on or after the international filing date
"L" document which may throw doubts on priority claim(s) or which is cited to establish the publication date of another citation or other special reason (as specified)
"O" document referring to an oral disclosure, use, exhibition or other means
"P" document published prior to the international filing date but later than the priority date claimed
"T" later document published after the international filing date or priority date and not in conflict with the application but cited to understand the principle or theory underlying the invention
"X" document of particular relevance; the claimed invention cannot be considered novel or cannot be considered to involve an inventive step when the document is taken alone
"Y" document of particular relevance; the claimed invention cannot be considered to involve an inventive step when the document is combined with one or more other such documents, such combination being obvious to a person skilled in the art
"&" document member of the same patent family

Date of the actual completion of the international search 26 February 2015 (26.02.2015)	Date of mailing of the international search report 25 MAR 2015
Name and mailing address of the ISA/ Mail Stop PCT, Attn: ISA/US, Commissioner for Patents P.O. Box 1450, Alexandria, Virginia 22313-1450 Facsimile No. 571-273-3201	Authorized officer Shane Thomas PCT Helpdesk: 571-272-4300 PCT OSP: 571-272-7774